

# Cooling rate of clinopyroxene reveals the thickness and effusion volume of Chang'E-5 basaltic flow units

Zilong Wang<sup>a,b</sup>, Wei-(RZ) Wang<sup>a,\*</sup>, Wei Tian<sup>b,\*</sup>, Huijuan Li<sup>b</sup>, Yuqi Qian<sup>c</sup>, Junling Pei<sup>a</sup>, Zhenyu Chen<sup>d</sup>, Dianbing Wang<sup>b</sup>, Ping-Ping Liu<sup>b</sup>, Wenzhe Fa<sup>b</sup>, Jiang Wu<sup>a</sup>, Hong Bao<sup>a</sup>

<sup>a</sup> Key Laboratory of Paleomagnetism and Tectonic Reconstruction of MNR, Institute of Geomechanics, Chinese Academy of Geological Sciences, Beijing 100871, China

<sup>b</sup> School of Earth and Space Sciences, Peking University, Beijing 100871, China

<sup>c</sup> School of Earth Sciences, China University of Geoscience, Wuhan 430074, China

<sup>d</sup> Key Laboratory of Metallogeny and Mineral Assessment of MNR, Institute of Mineral Resources, Chinese Academy of Geological Sciences, Beijing 100037, China

## ARTICLE INFO

### Keywords:

Chang'E-5

Mare basalts

Cooling rate

Lava flow thickness

Effusion volume

## ABSTRACT

China's Chang'E-5 mission landed in the northern Oceanus Procellarum and sampled the youngest mare basaltic regolith (1.9–2.0 Ga) to date. The returned samples enable us to gain new insights into the thickness and eruption volume of the basaltic flow unit, i.e., Em4, the fourth Eratosthenian-aged mare unit at the landing region. In this study, 1D bottom-up and top-down cooling and top-down-only cooling thermophysical models have been constructed for the emplacement of the Chang'E-5 flow unit in order to constrain its minimum thickness through the cooling rates. Based on the zoning profiles of Mg–Fe diffusion in clinopyroxene, the cooling rate of the coarsest-grained sample is constrained to be 0.00025–0.00055 K/h, corresponding to a flow unit with a minimum vertical dimension of 21–118 m. The minimum effusion volume of a single flow unit at the Em4 area is calculated to be 777–3626 km<sup>3</sup>, which indicates that the Em4 region where Chang'E-5 landed is mainly formed in one major effusion event. The large volume of the Chang'E-5 mare flow suggests that the mantle source of Chang'E-5 basalts in the Procellarum KREEP Terrane was warm enough to produce significant amounts of melt.

## 1. Introduction

Mare basalts are generated from the mantle, ascending and erupting through dikes (e.g. [Fagents et al., 2013](#); [Wilson and Head, 2017](#)). The effusion volume or rate of mare basalts during a single volcanic event could largely reflect the internal thermal state of the mantle, as a hot mantle would produce more melts to support the volcanism (e.g. [Shearer et al., 2006](#)).

The thickness of lava flows, which can be used to constrain the individual lava flow volume and the volume of partial melts produced in the mantle, is key to understanding the thermal history of the Moon (e.g. [Wieczorek et al., 2006](#)). Recently, the thickness and effusion volume of lunar basalts have been constrained through various remote-sensing techniques, including crater topographic profile (e.g. [Weider et al., 2010](#); [Chen et al., 2018](#); [Jia et al., 2021, 2022](#)), the knee point of crater size-frequency distribution (e.g. [Hiesinger et al., 2002](#)), crater excavation depths (e.g. [Hu et al., 2019](#); [Chen et al., 2018](#)), and degradation of partially buried craters (e.g. [Du et al., 2019, 2022](#); [Yang et al., 2021](#)). Alternatively, cooling rates of basalts can be used to quantify the

thickness and effusion volume of their parent flow unit (e.g. [Peck et al., 1977](#); [Hudgins et al., 2011](#); [Murri et al., 2019](#)). However, such attempts on lunar samples are limited because of few sample-return missions and a paucity of slow-cooling samples reported (e.g. [Walker et al., 1976](#); [Richter et al., 2021](#)).

Chang'E-5 is China's first lunar sample return mission. It landed on a mare unit (i.e., Em4, fourth Eratosthenian-aged mare unit at the landing region, [Qian et al., 2018](#)) in the northern Oceanus Procellarum with the youngest radiometric dating age reported thus far (~2.0 Ga, [Che et al., 2021](#); [Li et al., 2021](#)). This age establishes the Chang'E-5 basalts as one of the youngest mare basalts on the Moon ([Hiesinger et al., 2011](#)), much younger than any basalts dated before. As the eruption flux of the Moon decreases significantly after its formation due to secular cooling ([Hiesinger et al., 2011](#)), the thermal state of mare basalt reservoir in the later stage can be quite different from that in the earlier stage (e.g. [Yue et al., 2022](#)). Hence, constraints on the thickness and the effusion volume of Chang'E-5 basalts can shed new light on the late-stage thermal state of the Moon.

In this study, we constrain the minimum thickness of the individual

\* Corresponding authors.

E-mail addresses: [wangwei0521@gmail.com](mailto:wangwei0521@gmail.com) (W.-(R. Wang), [davidtian@pku.edu.cn](mailto:davidtian@pku.edu.cn) (W. Tian).

<https://doi.org/10.1016/j.icarus.2022.115406>

Received 8 August 2022; Received in revised form 18 December 2022; Accepted 20 December 2022

Available online 22 December 2022

0019-1035/© 2022 Elsevier Inc. All rights reserved.

flow unit of Chang'E-5 basalts, based on cooling rates recorded in coarse-grained Chang'E-5 basaltic sample CE5C0800YJYX013GP allocated by China National Space Administration (CNSA). This sample contains two lithic fragments, which were picked from lunar regolith scooped by the robotic arm onboard Chang'E-5 lander at the landing site. Combining with the area of the flow unit estimated by previous studies, we calculate the effusion volume of a single volcanic event at  $\sim 2.0$  Ga to constrain the thermal state of the Moon at that time.

## 2. Methods

TESCAN Integrated Mineral Analyzer (TIMA) was used to study the petrology and mineralogy of the sample. Electron Microprobe Analyzer (EPMA) analysis was used to obtain the major element compositions of the minerals. Cooling rates were modeled based on the diffusion zoning of clinopyroxene.

### 2.1. TESCAN integrated mineral analyzer (TIMA) analysis

The TIMA comprises a Tescan Mira Schottky field emission automated scanning electron microscopy (ASEM) system with four silicon drift energy-dispersive (EDS) detectors arranged at approximately  $90^\circ$  intervals around the chamber. The measurements were performed in high-resolution liberation analysis mode. BSE images were acquired to define individual particles and the boundaries between distinct phases. A rectangular mesh of X-ray spectral measurements was obtained for each specific phase. TIMA analyses were conducted at a 25 kV working voltage with a spot size of 110 nm, a working distance of 15 mm, and a field size of 1000  $\mu\text{m}$ . The modal abundances of phases were determined following the method described in [Stadermann et al. \(2022\)](#).

### 2.2. EPMA analysis

Major element compositions of the minerals were determined on a JEOL-JXA-IHP200 electron microprobe (EMP) at the Institute of Mineral Resources, Chinese Academy of Geological Sciences (CAGS). The working conditions were as follows: 15 kV accelerating voltage, 20 nA beam current, and 1–5  $\mu\text{m}$  beam diameter. Natural minerals and synthetic oxides were used as standards, and a program based on the ZAF procedure was used for data calibration. The error for all elements was below 5%.

Quantitative WDS analyses and  $K\alpha$  X-ray mappings of major elements were conducted using five WDS spectrometers simultaneously, with an accelerating voltage of 15 kV, a beam current of 30 nA, a spot size of 1  $\mu\text{m}$ . Dwell times were 60–180 ms and pixel sizes were 1–2 mm depending on the size of the mapped area. Standards were a mix of both natural and synthetic minerals and oxides, and the quality of analyses was assessed based on stoichiometric constraints.

The bulk composition was determined using the weighted average of EPMA composition and the modal abundance of all mineral phases determined from TIMA analyses, as described in [Hahn et al. \(2017\)](#).

### 2.3. Cooling rate calculations

#### 2.3.1. A growth-then-diffusion initial condition

Based on the assumption that the chemical zoning patterns are formed purely by diffusion, traditional diffusion chronometry model utilizes an initial condition of a step function determined by elemental concentrations of cores (C0) and rims (C1) (e.g. [Chakraborty and Dohmen, 2022](#)) ([Fig. 1a](#)). However, chemical zoning patterns are typically produced collectively by crystal growth and subsequent diffusive

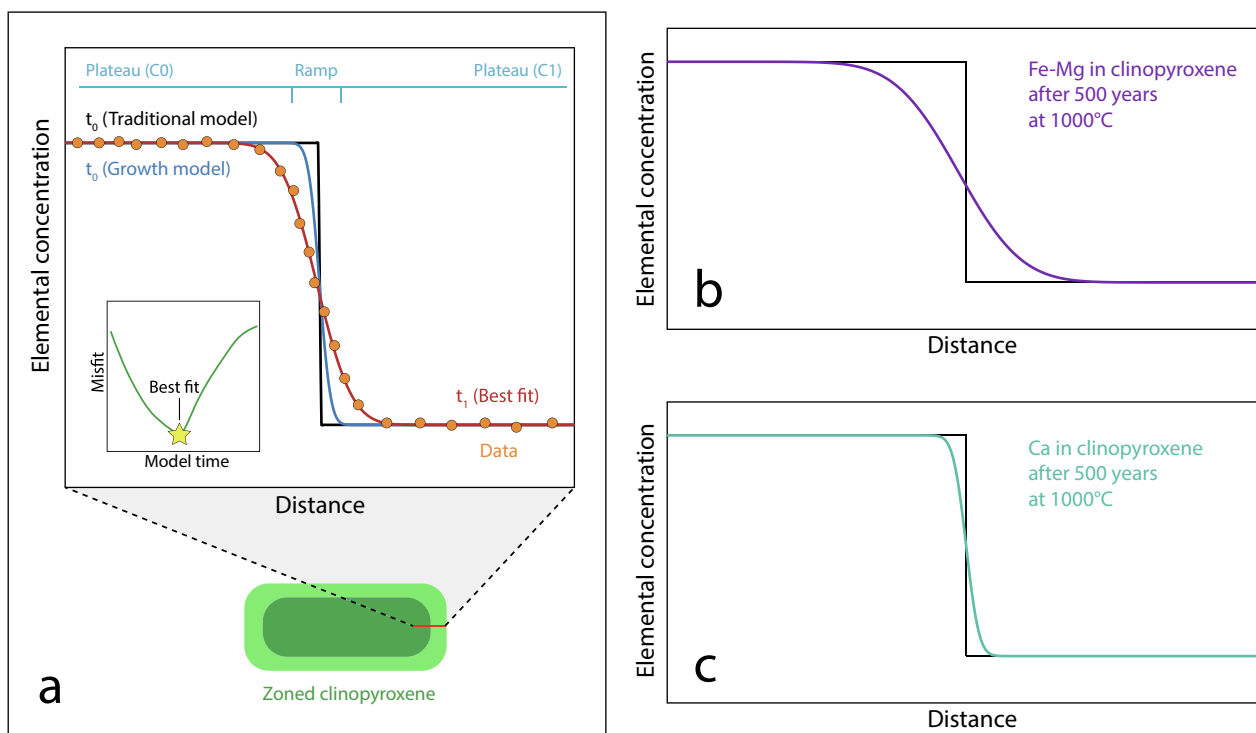


**Fig. 1.** A schematic illustration of growth-then-diffusion model, modified after [Brugman et al. \(2022\)](#). (a) Diffusive relaxation of element intracrystalline zoning in clinopyroxene. The black line (labeled “Traditional model”) shows the step function that is often used as the initial condition for diffusion modeling. In this work, the Ca concentration measured in clinopyroxene was used as a proxy for the growth-then-diffusion initial condition (blue line labeled “Growth model”). This initial condition was used as a starting point for modeling diffusive relaxation of Fe–Mg. An illustration of the present-day concentration of Mg# ( $\text{Mg\#} = \text{Mg}/(\text{Mg} + \text{Fe})$  in molar percent) measured in clinopyroxene is represented by the orange solid circle (labeled “Data”). The best fit (at the point of the minimal misfit) of measured data is indicated by red curve. (b) and (c) Comparison of synthetically-generated elemental concentration profiles for two elements that diffuse at different rates. Both Fe–Mg and Ca diffusion are modeled in clinopyroxene at 1000 °C with a traditional step function initial profiles. After the same amount of time, the profile of the faster diffusing Fe–Mg has considerably relaxed, relative to slower diffusing Ca.

relaxation (Costa et al., 2008). Taking crystal growth into consideration, an initial condition of traditional step-function may lead to an oversimplification for the diffusion timespan estimates. As such, it is essential to quantify the contribution of crystal growth and diffusive relaxation to the observed zoning profiles before the diffusion chronometry modeling. Such a quantification can be achieved by comparing the respective effects of growth and diffusion on zoning profiles, and specifically, by comparing slow-diffusing and fast-diffusing elements in a single crystal (e.g. Costa et al., 2020). If the chemical zonation of a mineral results from diffusion alone, the faster-diffusing elements should have longer ramps than slower-diffusing elements, after the same time span. As an example, Ca in clinopyroxene diffuses 1–2 orders of magnitude slower than Fe and Mg at the same temperature (Müller et al., 2013; Miyamoto and Takeda, 1994). Fig. 1b and c show the diffusion profiles for Fe–Mg and Ca in clinopyroxene, modeled at 1000 °C and using a step-function initial condition. After 500 years, the ramp of the Fe–Mg profile would be ~120 µm wide, while for the Ca profile it would be only ~20 µm wide. However, if crystal growth also contributes to the chemical zonation, concentration profiles of Ca and Fe–Mg would give discordant diffusive timescales using the traditional diffusion model (i.e. step-function initial condition). This is because the ramps of Ca profiles would be more sensitive to crystal growth because of their low diffusion coefficients, while the fast-diffusing Fe and Mg are more sensitive to diffusive relaxation. Therefore, the combination of Fe–Mg and Ca concentration profiles allows the growth profiles to be simulated and used as initial conditions for diffusion modeling. This modeling method was first introduced by Morgan and Blake (2006) and referred to as “binary element diffusion modeling” in that study. More recently, Brugman et al. (2022) further developed the method and described it as “growth-then-diffusion modeling”, which is used in this study (Fig. 1). We utilize the shape of the slow-diffusing element (Ca) to determine the initial condition when modeling the interdiffusion of fast-cooling element pair (Fe–Mg), as described in Brugman et al. (2022). The coupled diffusion of Fe and Mg are used for diffusion chronometry modeling in clinopyroxene, following previous literatures (e.g. Lierenfeld et al., 2019; Pelullo et al., 2022). In detail, all the EPMA data of Ca concentrations in clinopyroxene are firstly fitted to the error function at various modal time. Then, the standard deviations between the EPMA data and the modal error functions are calculated as “misfits”, and the best fit thus corresponds to the model time when the minimum misfit is reached (Fig. 1a). The details of Fe–Mg diffusion chronometry modeling are given in 2.3.2.

### 2.3.2. Modeling methods

The cooling rates can be constrained by mathematically computing the thermal diffusion equation (Fick’s law), that is

$$\frac{\partial C}{\partial t} = D(T) \frac{\partial^2 C}{\partial r^2} \quad (1)$$

where C refers to the elemental concentration at position r after time t, r is the distance from the center of the crystal ( $r = 0$ ), and D(T) is the temperature dependent diffusion coefficient. The boundary conditions are taken as follows:

$$\frac{\partial C}{\partial r} = 0, r = 0, r = A, t > 0 \quad (2)$$

where A is the radius of the crystal (assuming the crystal is concentric) (after Gao et al., 2011 and Miyamoto and Takeda, 1994). The initial conditions are based on the Ca concentration profile of each pyroxene grain, illustrated in Section 2.3.1 and shown in Section 3. In order to calculate the cooling rate ( $\Delta T/\Delta t$ ), one must know the cooling temperature intervals ( $\Delta T$ ). A new clinopyroxene thermometer (Wang et al., 2021) has been established for mafic magmatic systems and recalibrated using 559 experimental runs conducted in low pressures (from 1 bar to 12 kbar), which are consistent with lunar conditions. Using this thermometer, the crystallization temperatures of clinopyroxene cores and

rims are determined to be 1032–1086 °C and 950–1033 °C respectively (Fig. S1). Considering that the high temperature part of the cooling path dominates the diffusive evolution, the effect of diffusive relaxation below the final crystallization temperature of clinopyroxene rims (950 °C) is negligible (e.g. Mitsui et al., 2002; Dohmen et al., 2017). Therefore, we computed the Fe–Mg and Ca zoning profiles in clinopyroxene at various cooling rates from 1033 °C (1306.15 K) to 950 °C (1223.15 K). The effect of clinopyroxene orientation on the cooling rate calculation is also negligible, as the diffusion coefficients of Fe–Mg and Ca in clinopyroxene along the a and b axes are generally equal to that along the c axis within error (Figs. 3 and 4 in Zhang (2010)). Hence, the diffusion coefficients of Fe–Mg ( $D_{\text{Fe-Mg}} = 2.77 \times 10^{-7} \exp. (-320.7 \text{ kJ/mol/RT}) \text{ m}^2/\text{s}$ , Müller et al., 2013) and Ca ( $D_{\text{Ca}} = 3.81 \times 10^{-18} \exp. (-89.2 \text{ kJ/mol/RT}) \text{ m}^2/\text{s}$ , Miyamoto and Takeda, 1994) (all along the c axis) in clinopyroxene were utilized for the calculations.

The following criteria have been utilized for the choice of specific traverses in clinopyroxene: 1. The cracks in clinopyroxene should be avoided. 2. The clinopyroxene adjacent to olivine should not be chosen, as the Fe–Mg exchange between olivine and clinopyroxene may influence the precision of calculation results. 3. If mineral inclusions are present in some certain orientations of clinopyroxene, then the traverse should not be set along these orientations. 4. The traverses should be set along the steepest direction of ramp slopes and normal to the core-rim interfaces in clinopyroxene (e.g. Ganguly et al., 2000). As such, five traverses in five independent clinopyroxene grains have been chosen for growth-then-diffusion calculations.

### 2.4. Lava flow thickness estimation

Cooling rates based on chemical diffusion calculations of a sample can provide constraints on the size of the magma flow unit in which the sample is emplaced (e.g. Walker et al., 1976). However, previous studies based on such a method assumed heat loss involving only one nearby surface (Walker et al., 1976; Miyamoto and Takeda, 1994; McCallum et al., 2006; Mikouchi et al., 2012), probably resulting in serious underestimation of the thickness of a single flow unit. We use a method adapted from Hudgins et al. (2011) to simulate the heat transfer processes of a magma flow unit (i.e., predicting the temperature-field evolution within the magma flow over time) either when the flow is emplaced on ambient lunar soil or when the flow is emplaced onto a hot magma body immediately before the eruption of the studied flow. The thermal modeling was conducted using the finite element method software application COMSOL Multiphysics 6.0. Based on the possible occurrences of the magma body, we investigated the “bottom-up and top-down cooling” scenario (the flow is emplaced on ambient lunar soil and cooled on both sides), and the “top-down-only cooling” scenario (the flow is emplaced onto a hot magma body, which is similar to a dike or lava pool with heat supply from the bottom) respectively. The modeling details and the results are described below in Section 3.3.

## 3. Results

### 3.1. Petrology and mineralogy

The studied samples are basaltic fragments, characterized by coarse-grained (up to 1 mm) subophitic intergrowths of subhedral lathlike plagioclase, anhedral clinopyroxene, and euhedral needle-like ilmenite (Fig. 2). Olivine crystals are low in abundance, and are only present in clast 1 (Fig. 2c). The mineral modal abundances of the two clasts are shown in Fig. S2. Both clasts display a certain degree of shock-induced modifications, mainly as fracturing of most silicate minerals. Some plagioclase grains exhibit distinctive agglutinates and fusion crust, which are typical products of impact reheating (Fig. 2c). As shown by the comparison with the grain-size of all the other samples (in which mineral grains typically <200 µm in length) released from CNSA (see <https://moon.bao.ac.cn/moonSampleMode/index.html>), the samples

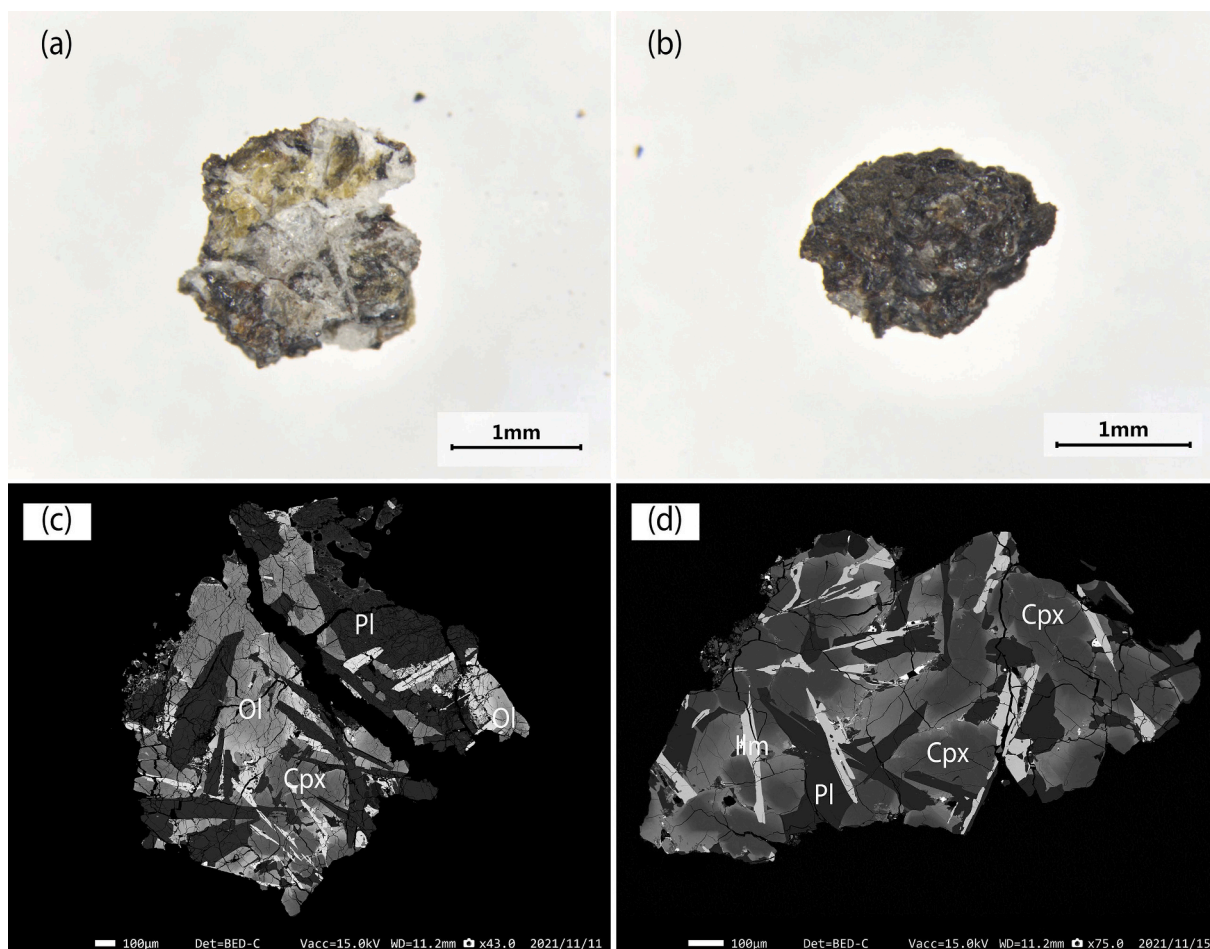


**Fig. 2.** Optical images (a, b) and back scattered electron (BSE) image (c,d) of CE5C0800YJYX013GP. (a, c) for clast 1, and (b, d) for clast 2. Cpx = clinopyroxene, Ol = olivine, Pl = plagioclase, Ilm = ilmenite.

(mineral grains typically  $\sim 500\text{--}1000\ \mu\text{m}$  in length) in this study are among the coarsest ones.

Pyroxene occurs as anhedral grains ( $\sim 500\ \mu\text{m}$  in length) (Fig. 2). All the pyroxene grains are clinopyroxene, strongly zoned from Mg-rich augite cores ( $\text{Wo}_{31-42}\text{En}_{29-37}\text{Fs}_{27-34}$ ) to Fe-rich pigeonite rims ( $\text{Wo}_{8-34}\text{En}_{1-30}\text{Fs}_{41-90}$ ) (Fig. S3a). Minor elements are also zoned from cores to rims (Fig. S3a). Al, Cr, and Ti display the same trend – their concentrations decrease from the core to the rim. All the referenced elemental zoning profiles are present as smooth-out step function zoning (Fig. S3a), indicative of diffusion-induced re-equilibration (Costa et al., 2008; Wenzel et al., 2021).

Olivine is larger (up to  $\sim 1\ \text{mm}$  in length), also normally zoned from Mg-rich cores ( $\text{Fo}_{53-54}$ ) to Fe-rich rims ( $\text{Fo}_{5-15}$ ) (Fig. S3b). Minor elements in olivine are slightly zoned. Ca and Ti contents increase slightly from cores to rims, and  $\text{P}_2\text{O}_5$  content increases a few folds from cores ( $\sim 0.03\ \text{wt}\%$ ) to rims ( $\sim 0.17\ \text{wt}\%$ ) (Fig. S3b). However, the elemental profiles for olivines in this study have much more flattened slope and do not follow the shape of the step-function zoning profile (Fig. S3b). This may be due to the much higher diffusion rate in olivine than that in clinopyroxene, as a result, the cores of olivine have undergone re-equilibration and do not represent their original composition (e.g. Hartley et al., 2016; Oeser et al., 2015; Shea et al., 2015).

Plagioclase occurs as euhedral to subhedral laths, up to  $\sim 1\ \text{mm}$  in length and  $200\ \mu\text{m}$  in width (Fig. 2). The grains have significant elemental zoning, with cores being relatively Ca-rich, Na- and K-poor ( $\text{An}_{85-87}\text{Ab}_{11-13}\text{Or}_{0.4-0.6}$ ) compared to the rims ( $\text{An}_{78-81}\text{Ab}_{16-19}\text{Or}_{1-2}$ ) (Fig. S3c). In addition, the FeO content ascends from core ( $0.3\text{--}0.5\ \text{wt}\%$ ) to rim ( $1.0\text{--}1.5\ \text{wt}\%$ ), whereas the MgO content descends from core

( $\sim 0.2\ \text{wt}\%$ ) to rim ( $<0.1\ \text{wt}\%$ ) (Fig. S3c). This may correspond to the enrichment of Fe and the depletion of Mg in the residual melt.

The mesostasis is extremely rare (modal abundance  $<1\%$ ), containing accessory quartz, troilite, apatite, merrillite, fayalite, K-feldspar, hyalophane, and Zr-bearing phases. The lack of mesostasis implies that the sample may originate from a thick lava flow, where the cooling rate is relatively low preventing the formation of mesostasis.

### 3.2. Cooling rates

Preliminary results from EPMA revealed that the ramps of Fe–Mg zonation in clinopyroxene ( $\sim 30\text{--}80\ \mu\text{m}$ ) are significantly longer than those of Ca zonation ( $\sim 10\text{--}20\ \mu\text{m}$ ), consistent with the lower diffusion coefficient of Ca than those of Fe and Mg. This indicates that diffusion indeed plays an essential role in the formation of chemical zonation in clinopyroxene. However, the ramp lengths of Fe–Mg profile are not positively correlated with those of Ca profile. For example, cpx-1 has ramp lengths of  $\sim 80\ \mu\text{m}$  and  $\sim 20\ \mu\text{m}$  for Fe–Mg and Ca profiles respectively, while cpx-2 has a much shorter ramp length for Fe–Mg profile ( $\sim 30\ \mu\text{m}$ ) but a similar length for Ca profile ( $\sim 20\ \mu\text{m}$ ) (Fig. 3). Such a variance of ramp lengths could not be plausibly explained without the consideration of crystal growth (e.g. Costa et al., 2020). That is, the concentration profiles of Fe–Mg and Ca across the boundaries of the intracrystalline zones of clinopyroxene recorded a growth-then-diffusion process, in agreement with our diffusion calculation method described in Section 2.3.

The observed chemical profiles and the regressed cooling curves of clinopyroxene are shown in Fig. 3. The calculated best-fit Ca profiles are

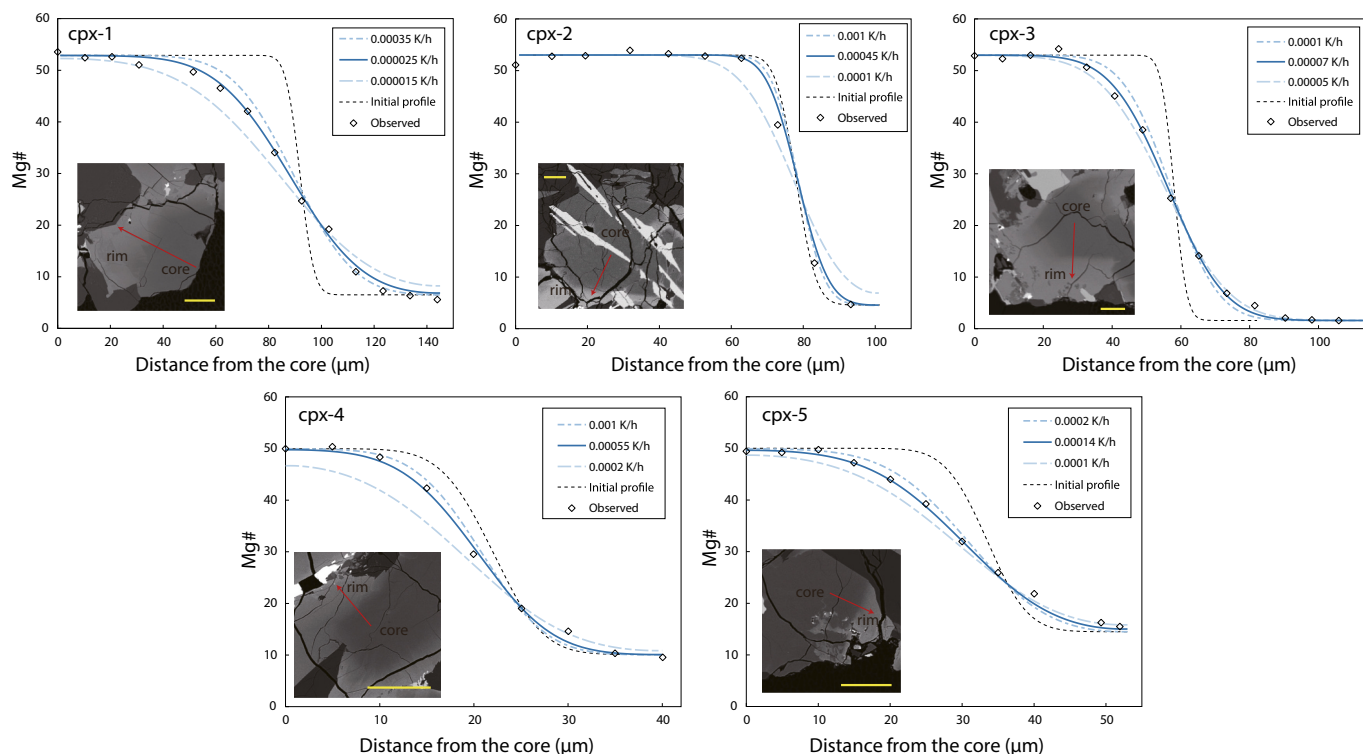


**Fig. 3.** Fe–Mg zonation in clinopyroxene and calculated diffusion curves at different cooling rates. Cpx-2 is from clast 1, and the other clinopyroxenes are from clast 2. In each panel, the best fit for the measured EPMA profile data is shown by solid blue curve. The black dotted curves denote the initial conditions for diffusion calculations. The red arrows indicate the direction of the EPMA measurement (from core to rim), and the yellow scale bars are 50  $\mu\text{m}$ . (For interpretation of the references to colour in this figure legend, the reader is referred to the web version of this article.)

shown in Fig. S4 and are regarded as the initial profiles before Fe–Mg diffusive relaxation (Fig. 3). The Fe–Mg zoning profiles of clinopyroxene are best fitted with cooling rates of 0.00025–0.00055 K/h. These values are typical for the emplacement of a thick lava flow (e.g. Yamaguchi et al., 2021), again consistent with petrological constrains of low cooling rates (see texts above).

In order to validate the cooling rate yielded from clinopyroxene Fe–Mg profiles, we also estimated cooling rates using the largest plagioclase crystal in clast 1 and the Mg-in-plagioclase speedometer (Faak et al., 2013, 2014; Dohmen et al., 2017). The plagioclase crystal exhibits chemical zonation with MgO content decreasing from core (0.23 wt%) to rim (0.08 wt%). Following the arguments of Faak et al. (2014), initial temperature used for calculations is the onset temperature of clinopyroxene core crystallization (1087  $^{\circ}\text{C}$ , Fig. S1), which corresponds to a final temperature (i.e. closure temperature) of 883  $^{\circ}\text{C}$  according to Eq. (5) in Faak et al. (2014). The calculation results indicate an estimated cooling rate of  $\sim 0.0005$  K/h (Fig. 4), broadly consistent with the cooling rate range (0.00025–0.00055 K/h) derived from clinopyroxene Fe–Mg diffusion calculations. Minor differences in cooling rates estimated by these two methods are probably due to the differences in modeling temperature range (950–1033  $^{\circ}\text{C}$  for clinopyroxene, 883–1087  $^{\circ}\text{C}$  for plagioclase), which is the main source of error in the timescale estimates (e.g. Bernard et al., 2022).

Based on the diffusion calculation results of Fe–Mg in clinopyroxene and Mg in plagioclase, the cooling rate of clast 1 is 0.00045–0.0005 K/h (based on 1 cpx profile and 1 plagioclase profile, Fig. 3 and Fig. 4), and the cooling rate of clast 2 is 0.00055–0.00025 K/h (based on 4 cpx profiles, Fig. 3). However, the lowest cooling rate (0.00025 K/h, from cpx-1) for the clast 2 may have a larger uncertainty, as the zoning of cpx-1 is more patchy than other clinopyroxenes (Fig. 3), possibly resulting in the traverses not measured normal to the interfacial plane. Traverses obliquely intersecting the plane have the length of the ramp longer than that for diffusion normal to the plane, therefore resulting in slower

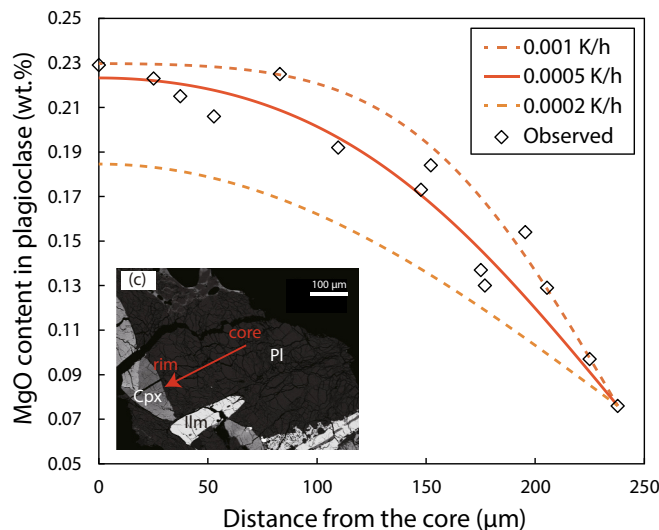


**Fig. 4.** Measured (black hollow diamonds) and fitted (orange lines) Mg-concentration profiles in plagioclase of the sample, indicative of a cooling rate of  $\sim 0.0005$  K/h.

cooling rates (e.g. Ganguly et al., 2000). In the 2D thin section one can only assure the direction with respect to the trace of the interface. Therefore, the highest cooling rate (0.00055 K/h) estimated from diffusion modeling is more likely to be the true cooling rate for clast 2. The cooling rate of clast 1 is therefore consistent with that of clast 2, possibly indicating that the two clasts may have undergone a similar thermal history.

### 3.3. Size estimates of the Chang'E-5 flow unit

#### 3.3.1. Bottom-up and top-down cooling scenario

There are two surfaces of heat loss combining to give the observed cooling rates in a lava flow with a finite thickness (Fig. 5). In this scenario, the heat inside the lava flow will be dissipated vertically upward and downward through thermal diffusion, producing the vertical temperature profile shown by the colored curves in Fig. 5b. Given the virtual absence of an atmosphere around the Moon, convective cooling was assumed to be negligible. As such, the boundary conditions specified at the Moon's surface were based solely on thermal radiation. The Stefan-Boltzmann law defines a radiative heat flux ( $q$ , measured in  $J/s/m^2$ ) from any object as Eq. (3):

$$q = \epsilon \sigma T^4 \quad (3)$$

where  $\epsilon$  is emissivity (a dimensionless parameter ranging from 0 to 1),  $\sigma$  is the Stefan-Boltzmann constant ( $5.6704 \cdot 10^{-8} J/s/m^2/K^4$ ), and  $T$  is temperature (K).

Conductive heat transfer was assumed in the underlying host rock. Although effect of thermal convection is significant when in liquid state, the magma was highly crystallized when the rims of clinopyroxene began to grow and thus conduction is still the dominant way of heat loss. Therefore, the equation of 1D conductive heat transfer by Fourier's law for an isotropic medium is employed here:

$$\frac{\partial T}{\partial t} = \frac{k}{\rho C_p} \frac{\partial^2 T}{\partial h^2} \quad (4)$$

where  $k$  is the thermal conductivity ( $W/m/K$ ),  $\rho$  is the solid density ( $kg/m^3$ ), and  $C_p$  is the specific heat capacity ( $J/kg/K$ ).

The geometry used for this scenario is illustrated in Fig. 5a. Input parameters are listed in Table 1 and all these parameters passed the sensitivity tests outlined in Hudgins et al. (2011). The model assumes average lunar-surface temperature  $T_{surf} = 212.15 K$  (Wesselink, 1948). The initial temperature of magma ( $T_0$ ) can be calculated using the whole rock MgO contents (Table S1) and the following equation:  $T$  (in  $^{\circ}C$ ) =  $26.3 \times MgO + 994.4$  (Putirka, 2008). Using this approach, the average MgO content (7.28 wt% and 4.58 wt%) estimated for the Chang'E-5 basaltic fragments equates to eruption temperatures of  $\sim 1186^{\circ}C$  and  $\sim$

**Table 1**

Material properties used for thermal modeling.

Parameters*	Values	Units	References
$T_{surf}$	212.15	K	
$T_0$	1423.15	K	
$\epsilon$	0.8		Arndt et al. (1979)
$k$	$2.4-9.53 \times 10^{-4} T$ (T is instantaneous temperature on the contact boundary)	W/m/K	Sakatani et al. (2018)
$\rho$	3200	kg/m <sup>3</sup>	Ishihara et al. (2011)
$C_p$	1250	J/kg/K	Zhang et al. (2013)

\* All parameters are for mare basalts.

$1115^{\circ}C$  respectively. Therefore, the average eruption temperature of  $1150^{\circ}C$  ( $1423.15 K$ ) is used as  $T_0$ . For simplicity it is assumed that the thermal diffusion coefficient of the crystalline magma is the same as that of the crustal host rock as they are all mare basalts with similar compositions (e.g. He et al., 2022). The model calculation considers only heat flux in the vertical direction and neglects the lateral heat, but this simplification is proved to be of insignificant effect on the evolution of the system (Hudgins et al., 2011; Richter et al. (2016) and references therein). Zero heat flux is assumed at the base of the model.

The calculated thermal profiles are exemplified in Fig. 5b. It is noted that the thermal profile in the shallower part of the lava flow is mainly affected by heat radiation, while the thermal profile in the deeper part of the lava flow is mainly affected by heat conduction. Hence, there are two positions always maintaining the same cooling rate in the lava flow. For example, position A and B are vertically  $\sim 40 m$  and  $\sim 70 m$  from the topmost of the lava layer, respectively. After a cooling timespan of 10 yr, the temperatures of A and B decrease simultaneously from  $T_s = 1306.15 K$  to  $T_e = 1223.15 K$  (from A and B to A' and B', Fig. 5b). Using the calculated thermal profiles, we can determine the vertical depth of A' relative to the topmost of lava layer ( $h_t$ ), and B' relative to the bottommost of lava layer ( $h_b$ ), respectively. The gross thickness of the lava layer (D) is thus.

$$D = h_t + h_0 + h_b \quad (5)$$

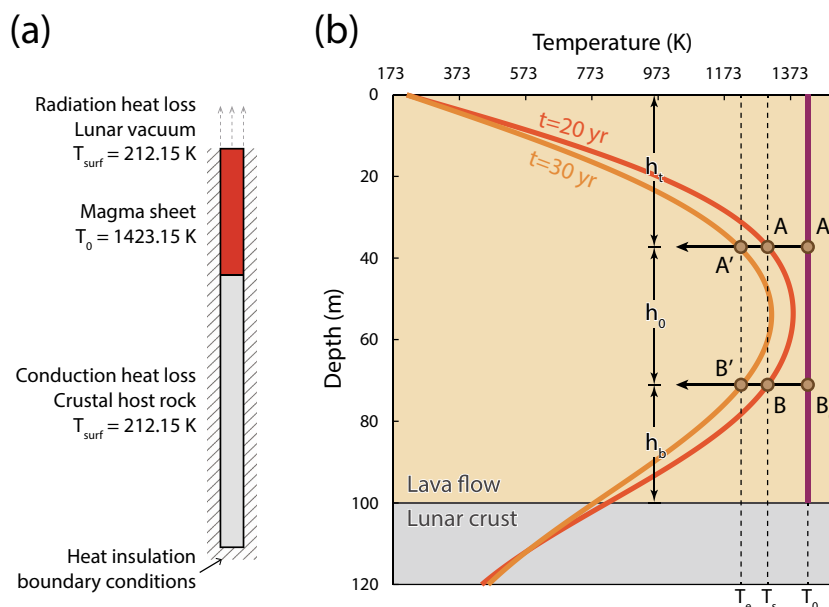


**Fig. 5.** (a) Geometry, boundary conditions and initial conditions used for 1D numerical modeling of heat transfer in the bottom-up and top-down cooling scenario. (b) The results of a simple diffusive thermal evolution model for a lava flow with a thickness of 100 m and an initial temperature  $T_0 = 1423.15 K$ , deposited on lunar cold surface at  $T_{surf} = 212.15 K$ .

where  $h_0$  is the vertical distance between A' and B', two points with the same cooling rate in the lava layer. The value of  $h_0$  cannot be estimated through thermal diffusion, hence

$$D \geq h_t + h_b, \text{ or } D_{\text{minimum}} = h_t + h_b \quad (6)$$

Although the exact location of the sample cannot be known, the expression of  $D_{\text{minimum}}$  means that the sample may originate from a position with the minimum cooling rate, which is obtained at the position along the thermal profile with the maximum temperature. A lava layer, which is thicker than the given one in Fig. 5, can have locations with a similar cooling rate, but a thinner layer cannot. Therefore, the minimum thickness of the layer would be the one which reproduces the cooling rate of the diffusion model at the maximum temperature along the profile. Too thin a layer would cool too fast everywhere, but even an infinitely large layer would have the desired cooling rate at some depth as a function of time. In summary, the sum of burial depths from the topmost and the bottommost of the lava layer ( $h_t + h_b$ ) provides a minimum estimation of the thickness of the lava layer.

Predicted cooling rate profiles for various lava flow thicknesses ( $D$ ) are shown in Fig. 6. In the case of a cooling rate of 0.00055 K/h, a lava flow thickness of  $\geq 118$  m is predicted (Fig. 6a). In the case of a cooling rate of 0.000025 K/h, the lava flow thickness is over 554 m (Fig. 6b). Thinner lava flows would produce faster cooling rates (Fig. 6). Therefore, in the bottom-up and top-down cooling scenario, the thickness of lava flow should be no  $< 118$ –554 m.

### 3.3.2. Top-down-only cooling scenario

The bottom-up and top-down cooling scenario assumes that the elemental diffusion between the cores and the rims of clinopyroxene commenced when the Chang'E-5 parent magma has been extruded and cooled as a lava flow on the lunar surface. However, if the extruded magma cooled in a lava pond or a lava lake, heat supply through magma conduit would result in no heat loss from the lower surface of the magma, as shown in Fig. 7a. Therefore, heat can only be lost upward, and the temperature of the magma decreases monotonically from the bottom to the top (Fig. 6b).

In order to further illustrate this scenario, we assume a position A within the heat-supplied magma with an initial temperature  $T_0 = 1423.15$  K and a burial depth of  $h_t = 35$  m (Fig. 7b). After a cooling timespan of 20 yr, the temperature of A decreases from  $T_s = 1306.15$  K to  $T_e = 1223.15$  K (from A to A', Fig. 7b). We can obtain the following relationship between the burial depth ( $h_t$ ) and the minimum magma size ( $D'$ ) graphically from Fig. 7b:

$$\frac{T_e - T_{\text{surf}}}{T_0 - T_{\text{surf}}} = \frac{h_t}{D'} \quad (7)$$

$D' = D$  ( $D$  is the true size of the magma) would be achieved only if the interior temperature profile of the magmatic body reaches an equilibrium state, i.e., the thermal profile of a finite-size heat-supplied magma after infinite-time cooling (green line in Fig. 7b).

Various methods for solving the burial depth ( $h_t$ ) of the sample in the top-down-only cooling scenario have been well-established and widely utilized by the community (e.g. Winkler, 1949; Jaeger, 1957; Grove and Walker, 1977; Mikouchi and Miyamoto, 2002; Mikouchi et al., 2012; Richter et al., 2016). One of the most practical methods for the planetary sample is based on the relationship  $h_t = C \times \sqrt{t}$ , where  $t$  is the cooling timespan and  $C$  is a constant dependent on the thermal diffusivity (e.g. Grove and Walker, 1977). McCallum and O'Brien (1996) solved the  $C$  value as  $5.2 \pm 1$  (when  $t$  is in years and  $h_t$  is in meters) for lunar samples based on the summary of thermal experiments and previous models. Utilizing the minimum  $C$  value (4.2), the calculated burial depths for the sample are 17.4 m and 81.8 m, at the cooling rates of 0.00055 K/h and 0.000025 K/h, respectively. Using Eq. (7), the minimum magma size is calculated to be within the range of 20.8–97.7 m.

It is noted that this scenario postulates that the lava pool/lake was

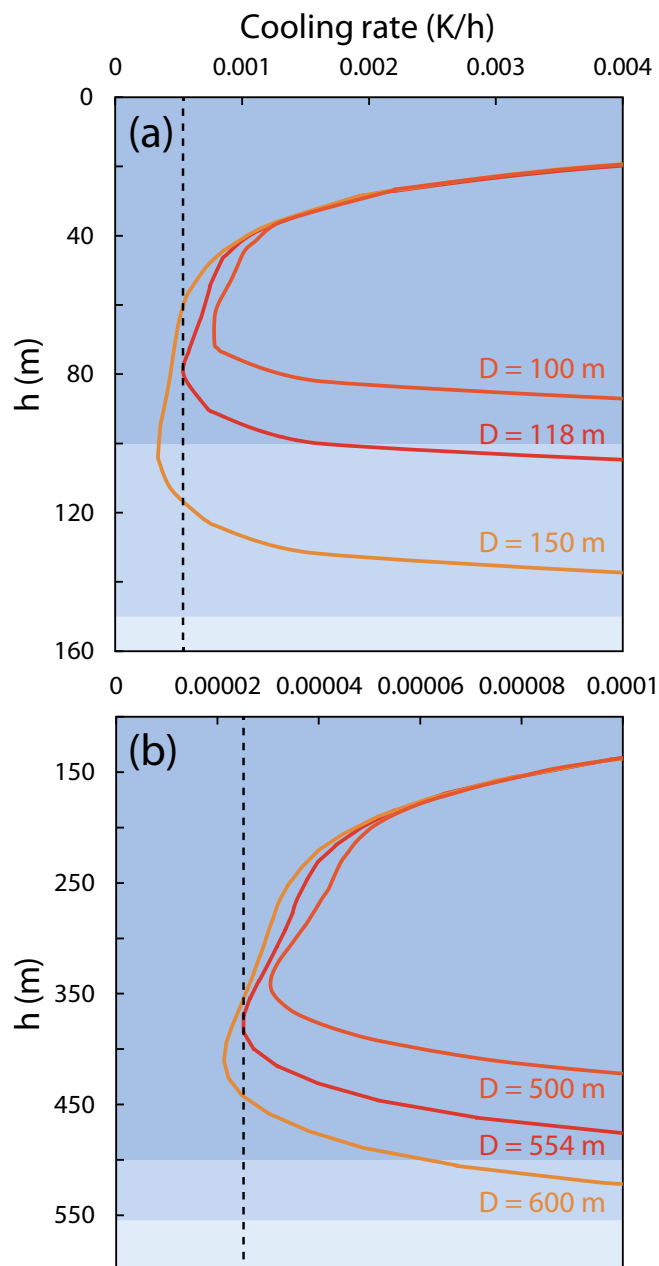


Fig. 6. Thermal profiles of the magmatic body at cooling rates of (a) 0.00055 K/h and (b) 0.000025 K/h (dashed line in each panel). The solid curve shows the calculated thermal profiles of the magmatic body at different sizes ( $D$ ). The ordinate ( $h$ ) is the distance from the top of the magmatic body.

large enough, so that the temperature of the heat source remained constant with time (Fig. 7b). Therefore, the minimum magma size calculated in this scenario can only be regarded as an extreme case. Conversely, if the temperature of the heat source also decreased during cooling, the actual case would be intermediate between the bottom-up and top-down scenario and the top-down-only scenario. Correspondingly, the minimum magma size obtained in the hybrid scenario would also be intermediate (i.e. between 20.8– and 97.7 m and 118–554 m).

## 4. Discussion

### 4.1. Chemical zonation in clinopyroxene and olivine

In our samples, some clinopyroxene cores have patchy zoning and

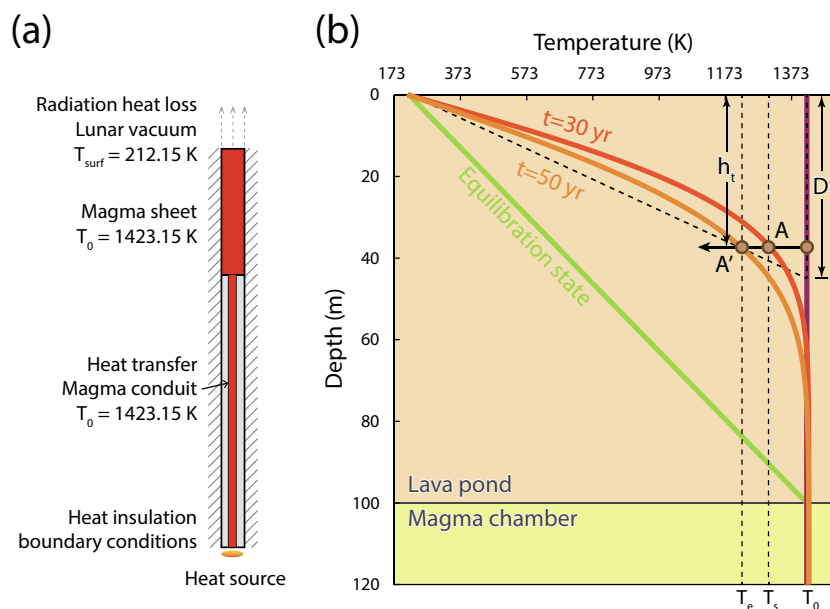


**Fig. 7.** (a) Geometry, boundary conditions and initial conditions used for 1D numerical modeling of heat transfer in the top-down-only cooling scenario. (b) The results of a simple diffusive thermal evolution model for magma with a heat supply, a depth of 100 m and an initial temperature  $T_{\text{mag}} = 1423.15$  K, deposited on lunar cold surface at  $T_{\text{surf}} = 212.15$  K.

ragged boundaries (e.g. cpx-1 and cpx-5 in Fig. 3), which are also observed in clinopyroxene grains of other extraterrestrial samples (e.g. Hui et al., 2011; Udry et al., 2017; Wenzel et al., 2021). This texture is usually interpreted as mild resorption of clinopyroxene cores due to physical environment change or diffusive re-equilibration. In the case of plagioclase, patchy zoning is usually attributed to polybaric crystallization, as the melting point would decrease with falling pressure faster than the adiabatic decrease of magma temperature, especially in water-deficient system (e.g. Vance, 1965). Patchy zoning in clinopyroxene, however, results usually when step-zoned crystals with homogenous cores are in the process of being slowly eliminated by diffusive relaxation during slow cooling (Streck (2008) and references therein). WDS Fe and Mg X-ray maps of the two studied clasts imply that the core and rim regions of clinopyroxene are rather homogeneous, with distinct Fe–Mg zonation between cores and rims (Fig. S5). Besides, EPMA traverse data also indicate that the Fe–Mg profiles of clinopyroxene have very similar shapes with only small differences between core and rim compositions, regardless of the adjacent phases at the start and end of the profile (Fig. 3). As such, texture and elemental distributions of clinopyroxene indicate that the coupled diffusion of Fe and Mg is a good proxy for the chronometry modeling in this study.

The Ca profiles in clinopyroxene, however, appear to be more complex and variable compared to the Fe–Mg profiles (Fig. S4). A prime example is the cpx-3, which presents an odd “double” Ca profile (Fig. S4). WDS Ca X-ray maps further reveal that Ca is mostly enriched in the mantle region instead of the core region in some clinopyroxene grains (Fig. S5). This may be because the Ca content during crystallization could be affected by fluxes from other directions oblique to the direction of the profile. Such fluxes could result from co-crystallization of other Ca-compatible minerals, e.g. plagioclase and phosphates, as indicated by Ca X-ray map (Fig. S5). Therefore, it appears to be implausible to assume zero flux of Ca in the crystal’s surface during crystallization. This indicates that the complex Ca profiles in clinopyroxene are largely attributed to crystal growth controlled by varying fluxes to other Ca-rich phases, instead of simple diffusive relaxation.

We calculate pressure and temperature (P–T) using the new clinopyroxene thermobarometer of Wang et al. (2021). The P–T results reveal that the clinopyroxene cores were crystallized within a P–T range of 0–3 kbar and 1046–1087 °C (with a  $dT/dP$  of 13 °C/kbar), while the rims

were crystallized at a temperature range of 950–1033 °C at ~0 kbar (Fig. S1). These P–T estimations support that the cores of clinopyroxene were crystallized in a subsurface crustal magma chamber (<3 kbar or < 60 km depth), while the rims were crystallized at lunar surface. Therefore, the change in composition between cores and rims is probably driven by a pressure change, most likely due to magma ascending (e.g. Hui et al., 2011). Also, it is noted that the predicted P–Ts of diffusion zones (between cores and rims) are anomalous, with unusually high pressures (up to 5–8 kbar) and apparent deviation from the P–T evolution line (13 °C/kbar) indicated by the core chemistry (Fig. S1). This probably indicates that the elemental diffusion could substantially affect the P–Ts (especially P) estimated using thermobarometers.

The cores of olivine in the sample appear to have been substantially modified by late-stage re-equilibration. In almost all the Chang’E-5 basalt samples, the grain size of olivine ranges from several hundred microns to almost 1 mm, remarkably larger than other minerals particularly in fine-grained samples (e.g. Fig. 2 in Jiang et al. (2021)). This is consistent with the early crystallization and subsequent fractionation of olivine from parental magma of Chang’E-5 basalts. However, we have no idea about the real original compositions of the olivine in Chang’E-5 basalts hitherto. In previous literatures, olivine grains in coarser-grained Chang’E-5 basalt samples usually have lower Fo values (e.g.  $Fo_{43-44}$ , Che et al., 2021), while higher Fo values in finer-grained samples (e.g.  $Fo_{60-61}$ , Tian et al., 2021; Jiang et al., 2021; He et al., 2022). In addition, Li et al. (2021) reported olivine with a Fo value of up to 65.1 in Chang’E-5 basaltic regolith, and He et al. (2022) argued olivine in Chang’E-5 basalts could have an even higher Fo value of 67, using MELTS algorithm and bulk compositions of their samples. Nonetheless, the evolved olivine Fo values and the correlation between grain size and specific olivine Fo value indicates that diffusive relaxation has appreciably modified the initial core compositions of olivine. The subdued slope of elemental profiles observed in our samples also supports the diffusive modification of core compositions in olivine (Fig. S3).

The crystallization of olivine rims is more enigmatic compared to that of the cores. The width of olivine rim is highly variable even in the same crystal, from up to 200  $\mu\text{m}$  to almost absent (Fig. S5). The rim also exhibits unusual textures, for example, the presence of abundant mineral and multiphase melt inclusions and ragged, reabsorbed rim structures (Fig. 2). Also, the CIPW Norm calculation using the bulk

composition of olivine-bearing clast (clast 1) reveals that the clast should have an ideal modal abundance of 11.6% for olivine, which is only half of the observed olivine modal abundance (24.2%) (Fig. S2; Table S1). These petrographic observations may suggest a solid-liquid or solid-solid reaction between the original olivine grains and residual melt or adjacent phases, forming the rim regions of olivine. Such a chemical reaction is induced possibly by magma mixing, or very likely, by late-stage liquid immiscibility, as suggested by He et al. (2022). Besides, impact-induced remelting may also result in low-degree partial melt, which are enriched in SiO<sub>2</sub>, FeO, and incompatible elements and thus could react with original olivine intercumulus, forming rim regions and the observed chemical zoning in olivine. The possibility of impact remelting is suggested by Long et al. (2022), who reported that the Chang'E-5 basalts have been severely impacted since their formation, resulting in significant amounts of impact glass formed in at least 17 independent impact events.

#### 4.2. Cooling-rate comparisons with previous studies

All the lunar sample return missions reveal that even in the same sampling site, the textures of different mare basalts are highly variable (e.g. Brown et al., 1975; Shearer et al., 2006), and the case of Chang'E-5 basalts is not an exception (Tian et al., 2021; Li et al., 2022). This is mainly due to the variation of relative emplacement depths among different mare basalts (e.g. Papike et al., 1976; Lofgren et al., 1981; Shearer et al., 2006). Hence, the determination of cooling rates is crucial for the understanding of the petrogenesis of different lunar basalts, as the cooling rate is controlled by the emplacement depth (Eqs. (6) and (7)). Many methods have been utilized for the cooling rate estimation of mare basalts for decades, including crystallization experiments, cooling-history geospeedometers, crystal-size distributions (CSD), and diffusion calculations (e.g. Richter et al., 2021; Stanin and Taylor, 1979; Grove, 1982; Donohue and Neal, 2015; Xue et al., 2021) (Fig. 8). Here, we review and compare the previous cooling-rate studies of Apollo, Luna and Chang'E-5 mare basalts, in order to access the optimum method for cooling-rate approximation of samples with distinct cooling rates.

Crystallization experiments and cooling-history geospeedometers derived from crystallization experiments are the most straightforward ways to determine the cooling rates of fast-cooling samples. Many works have successfully reproduced the textures presented in fast-cooling Apollo mare basalt samples through crystallization experiments (e.g. Stanin and Taylor, 1979; Lofgren et al., 1975; Grove, 1982; Donaldson et al., 1975). Stanin and Taylor (1979) estimated that Apollo-17 Type I basalts formed at a slower cooling rate ( $\sim 0.5$  °C/h), and Type II basalts formed at a faster cooling rate ( $\sim 5$  °C/h). Lofgren et al. (1975) and Grove (1982) reported the cooling rates of Apollo-15 low-Ti basalts range from  $<1$  °C/h to  $\sim 20$  °C/h. Donaldson et al. (1975) reported the Apollo-12 olivine vitrophyres cooled at rates of 10–100 °C/h, whereas the Apollo-12 olivine basalts cooled at rates  $<15$  °C/h, and the Apollo-12 olivine gabbros at rates  $<2.7$  °C/h (Fig. 8). However, the cooling rates of much slower cooling samples cannot be determined by crystallization experiments, or cooling-history geospeedometers. This is because the textures of slow-cooling samples may not be reproduced straightforwardly due to the limitations of experimental techniques, and thus the paucity of experimental calibrations leads to the inapplicability of cooling-history geospeedometers. For example, experimentally modeling a cooling rate of 0.1 °C/h requires  $\sim 4$  months of continuous cooling from liquidus to solidus, which is a significant challenge for the stability of experimental instruments and the cost of the experiments.

CSD method, which estimates the cooling rates by counting the size and quantity distributions of euhedral minerals, have also been pervasively utilized on Apollo mare basalts and lunar meteorites previously (e.g. Donohue and Neal, 2015; Xue et al., 2021). The cooling rates of different Chang'E-5 basaltic clasts were modeled through the size-distribution of ilmenite and plagioclase, yielding a cooling-rate range from  $\sim 1$ –2 °C/h to 86 °C/h (Neal et al., 2022; Webb et al., 2022)

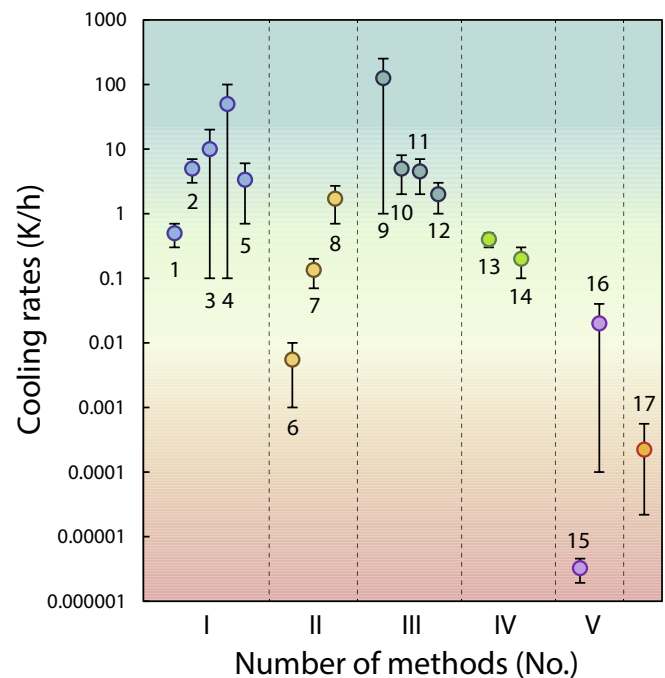


Fig. 8. The range of cooling rates determined for lunar samples through various methods. I—crystallization experiments; II—cooling-history geospeedometers; III—CSD method; IV—elemental-diffusion calculations of olivine; V—elemental-diffusion calculations of pyroxene. The values of cooling rates are cited from: 1: Apollo-17 Type I basalts in Stanin and Taylor (1979); 2: Apollo-17 Type II basalts in Stanin and Taylor (1979); 3: Apollo-15 low-Ti basalts in Lofgren et al. (1975); 4: Apollo-12 olivine basalts in Donaldson et al. (1975); 5: Apollo-12 basalt 12,032,366–18 in Stadermann et al. (2022); 6: Apollo-15 basalt 15,058 in Grove and Walker (1977); 7: mare basalt meteorite MIL 05035 in Joy et al. (2008) and Liu et al. (2009); 8: Chang'E-5 basalt 065 in Jiang et al. (2021); 9: Apollo-17 high-Ti basalts in Donohue and Neal (2015); 10: Apollo-11 high-Ti basalts in Xue et al. (2021); 11: Chang'E-5 basalt 329 in Neal et al. (2022); 12: Chang'E-5 basalt B1 in Webb et al. (2022); 13: Apollo-12 basalt 12,002 in Taylor et al. (1977); 14: Apollo-15 basalt 15,555 in Richter et al. (2021); 15: Apollo-17 gabbro 76,255 in McCallum et al. (2006); 16: Apollo-17 pigeonite basalt in Sanford and Huebner (1979); 17: Chang'E-5 basalt in this study.

(Fig. 8). However, the CSD method tends to overestimate the cooling rates of slow-cooling samples, as euhedral minerals record the cooling rate at the early stage of the magmatic crystallization, which can be 3–4 orders of magnitude higher than that at the late stage of crystallization (e.g. Jones et al., 2018). Wilson et al. (2022) also indicates that the cooling rate of Chang'E-5 parent magma can reach  $10 \pm 5$  °C/h at  $>1100$  °C, while decrease to  $9 \pm 3$  °C/yr ( $\sim 0.001$  °C/h) to lunar ambient below 1100 °C, by the study of lava flow mechanics.

Elemental-diffusion calculations of silicate minerals are also typical methods for determining the cooling rates of terrestrial and lunar samples (e.g. Chakraborty and Dohmen, 2022; Dohmen et al., 2017; Zhang, 2010). Recently, the estimate for the cooling rate of Apollo-15 olivine-normative basalt 15,555 yielded 0.2 °C/h, using Li diffusion in pyroxene (Richter et al., 2021). However, impact reheating process could have significantly affected the Li profile of pyroxene in the sample. The partial-melting texture of plagioclase in the sample indicates that the peak reheating temperature has once reached  $\sim 1763$  K (melting temperature of plagioclase with a composition of An<sub>80</sub>, Toramaru, 2022) for at least several seconds. On the other hand, the diffusion coefficient of Li in pyroxene at 1763 K is  $\sim 4 \times 10^{-5}$  cm<sup>2</sup> s<sup>-1</sup> (Richter et al., 2021), 8 orders of magnitude higher than that of Fe–Mg in pyroxene ( $9.1 \times 10^{-13}$  cm<sup>2</sup> s<sup>-1</sup>, Müller et al., 2013) at the same temperature. In this case, the Li profile of pyroxene with a length of  $\sim 500$  μm will be fully reset if the duration of 1763 K impact reheating exceeds  $\sim 60$  s ( $t = L^2/D_T$ , where  $t$

is the diffusion timespan,  $L$  is the diffusion length and  $D_T$  is the diffusion coefficient at a given temperature  $T$ ; Zhang, 2010), while the Fe–Mg profile remains unaffected during such a short reheating process.

Therefore, only the diffusional calculations of low diffusion-coefficient elements (e.g. Fe–Mg and Ca) in pyroxene can provide information on the cooling rates for slow-cooling samples (Fig. 8). The diffusion process commences after the crystallization of clinopyroxene rims; hence, the cooling rate ( $\sim 0.00025$ – $0.00055$  K/h) calculated in this study represents the cooling rate of the Chang'E-5 magma at the late stage of crystallization. This is important for the estimation of the emplacement depth of the sample in the lava flow, as the late-stage cooling rate directly depends on the final emplacement depth of the sample. Our calculated cooling rate is also consistent with results yielded through lava flow mechanics modeling by Wilson et al. (2022), which suggests that the sample in this study is derived from the deep interior of Chang'E-5 magma flow unit and thus suitable for the size constraint of the flow unit. In contrast, the fast-cooling Chang'E-5 basaltic fragments reported by Webb et al. (2022) and Neal et al. (2022) (Fig. 8) may represent the top layer of the Em4 mare flow. This interpretation is corroborated by the high abundance of mesostasis in those samples (He et al., 2022).

#### 4.3. Implications for the effusion volume of a single flow unit

By considering different styles of magma emplacement, we constrain the thickness of individual Chang'E-5 lava flow unit to be  $>118$ – $554$  m or  $>21$ – $98$  m, depending on the existence or nonexistence of a heat supply. Previous studies also suggested a similar size ranging from 39–to 61 m (Qian et al., 2021b) to 130–180 m (Du et al., 2019), based on the morphometry of craters in Chang'E-5 lava flow unit. More recently, Jia et al. (2022) estimated the thickness of Chang'E-5 mare basalt unit varies from  $\sim 15$  to  $\sim 50$  m through the excavation depth of craters. By contrast, Du et al. (2022) indicated 4-layer basaltic lava flows in the landing region and a much greater range of thickness: 9–175, 11–167, 19–478, and 0–800 m respectively. These results lead to the question about the thickness and volume of the total lava layers (cooling units) and a single lava layer of Chang'E-5 basalts.

The substantial differences in basalt thickness obtained by different methods may suggest two distinctive genesis models: multiple-magma-pulse model and single-magma-pulse model (Fig. 9). In the former model, the Chang'E-5 basalts are formed by at least two volcanic effusion events at short intervals, induced by discontinuous magma injection

in the chamber. The early-effused lava flow would be subsequently buried by the late-effused lava flow during cooling. In this case, our sample may originate from the early-effused lava flow, which have been overlain shortly after effusion to the lunar surface. As such, the relative thick lava flow ( $>118$ – $554$  m) indicated by the thermal model is more likely to reflect the total thickness of multiple lava layers (Fig. 9a). In the latter model, the Chang'E-5 basalts are formed mainly by a single major volcanic effusion event. The major effusion event may sustain for a long time, resulting from stable heat supply through the magma conduit. In this case, the thermal model in this study indicates a much thinner lava layer ( $>21$ – $98$  m) (Fig. 9b).

Using the Em4 area of  $\sim 37,000$  km<sup>2</sup> and the estimated thickness of the single lava layer ( $>21$ – $98$  m), the effusion volume of a single cooling unit of Chang'E-5 basalts is thereby at least  $777$ – $3626$  km<sup>3</sup>. This range is broadly consistent with the effusion volume ( $100$ – $2000$  km<sup>3</sup>) of a discrete volcanic event of sinuous rilles (Wilson and Head, 2017) and estimates for the total volume of the Chang'E-5 basalts from Qian et al. (2021b) ( $1450$ – $2350$  km<sup>3</sup>), while larger than the effusion volume ( $<1$ – $1000$  km<sup>3</sup>) of terrestrial basalts (e.g. Self et al., 1998; Gudmundsson, 2020). Considering that the heat supply from the chamber does not necessarily effectuate throughout the cooling process of Chang'E-5 basalts, the estimated effusion volume ( $777$ – $3626$  km<sup>3</sup>) can only be regarded as the minimum volume of a single cooling unit. This indicates that the Em4 region where Chang'E-5 landed was formed mainly by sheet flows fluxed in one major effusion event. Our finding is also consistent with the volume and morphology of the “Phase 1” high-flux sheet flows proposed in Qian et al. (2021a).

The effusion volume of a single cooling unit of Chang'E-5 basalts ( $>777$ – $3626$  km<sup>3</sup>) is also comparable to previous studies of mare basalts from different ages or sites. Using Clementine multispectral data, Weider et al. (2010) indicated that the individual lava flow unit with an age of 3.4–3.5 Ga could reach a volume from 340–to 620 km<sup>3</sup> to 4545–6100 km<sup>3</sup>. Hu et al. (2019) estimated the individual volume of 7 lava flow units at 1.1–3.2 Ga in Oceanus Procellarum and reported a value range of 569–3507 km<sup>3</sup>. Hiesinger et al. (2002) estimated the volume of individual lunar mare flow units in several lunar nearside basins as  $\sim 30$ – $7700$  km<sup>3</sup>, using the knee point of crater size-frequency distribution (CSFD). Chen et al. (2018) additionally employed the topographic profile analysis method to study the total effusion volume of basalts at  $<3.1$  Ga in Mare Imbrium, with an estimated value of  $\sim 8671 \pm 320$  km<sup>3</sup>. Therefore, the lava flow unit of Chang'E-5 basalts has an effusion volume in the same order of magnitude but slightly smaller than the

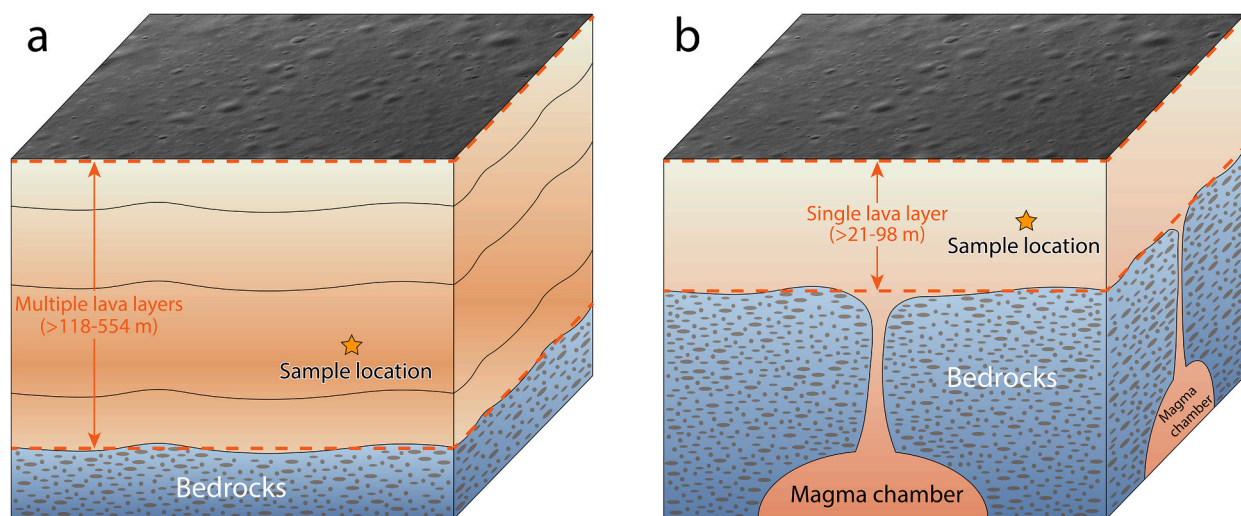


Fig. 9. Schematic genesis model of the Chang'E-5 basalts. (a) multiple-magma-pulse model, in which at least two discrete effusion events formed multiple lava layers at the Chang'E-5 landing region. (b) single-magma-pulse model, in which one major effusion event formed Chang'E-5 basalts, with stable heat supply from magma chamber. Not all features in this figure are shown at the same scale.

largest flow units with older ages (e.g. 3.4–3.5 Ga). This finding suggests that although the late-stage (<2.0 Ga) lunar volcanic activities have waned due to secular cooling (Zhang et al., 2013), it still maintained a high intensity to form the observed high effusion volume.

Under the assumption that only <0.1% of the magma source reached the lunar surface through dikes (Wilson and Head, 2017; Chen et al., 2018), the melt volume at source region is estimated to be at least  $8\text{--}40 \times 10^5 \text{ km}^3$ . Hence, large volumes of mantle materials ( $>8\text{--}40 \times 10^5 \text{ km}^3$ ) beneath the Chang'E-5 basalts should remain above its solidus in temperature ( $\sim 1300 \text{ }^\circ\text{C}$ ; Wicczorek and Phillips, 2000). Previous studies reported lunar mantle temperatures vary broadly from  $\sim 700 \text{ }^\circ\text{C}$  to  $\sim 1500 \text{ }^\circ\text{C}$  (e.g. Gagnepain-Beyneix et al., 2006; Khan et al., 2014; Zhang et al., 2019 and references therein). Our results indicate that at least part of the lunar mantle could have high temperatures around the solidus at  $\sim 2.0$  Ga, probably in a heterogenous internal heating scenario (Zhang et al., 2022), and thus have supported the eruptions in the Procellarum KREEP Terrane at that time. The results help to improve our understanding of the late-stage cooling history and the spatial distribution of internal heating of the lunar mantle.

## 5. Conclusions

- (1) Elemental compositions of clinopyroxene in Chang'E-5 mare basalts exhibit normal zoning resulting from crystal growth followed by diffusion.
- (2) The cooling rate is calculated from clinopyroxene Fe–Mg diffusion zoning in coarse-grained samples to be  $0.000025\text{--}0.00055 \text{ K/h}$ , consistent with that determined by Mg-in-plagioclase speedometer ( $\sim 0.0005 \text{ K/h}$ ).
- (3) A single flow unit sampled at the Chang'E-5 landing site has a minimum vertical size of 21–98 m, and the gross thickness of multiple lava layers is probably larger than 118–554 m.
- (4) The minimum effusion volume of Chang'E-5 basalts at a single volcanic event is estimated to be  $777\text{--}3626 \text{ km}^3$ , indicating that the Em4 region was possibly formed in one magma effusion event.
- (5) The mantle source region of the Chang'E-5 basalts in the Procellarum KREEP Terrane appears to be hot enough at  $\sim 2.0$  Ga, to produce significant amounts of melt ( $8\text{--}40 \times 10^5 \text{ km}^3$ ).

## Declaration of Competing Interest

The authors declare that they have no known competing financial interests or personal relationships that could have appeared to influence the work reported in this paper.

## Data availability

Data will be made available on request.

## Acknowledgements

The authors would like to thank Kayla Iacovino and Ralf Dohmen for their thorough and constructive reviews, and Doris Breuer for her constructive comments and detailed editorial works. The authors thank CNSA for providing the Chang'E-5 samples. The authors thank Tingnan Gong and Zuolin Tian for assisting EPMA and TIMA analysis, and Feng Liu, Jianen Han and Longyao Chen for their help during sample application and analysis. This research was financially supported by the National Natural Science Foundation of China (Grant Number 42272348 & 42172068).

## Appendix A. Supplementary data

Supplementary data to this article can be found online at <https://doi.org/10.1016/j.icarus.2022.115406>.

## References

- Arndt, J., Flad, K., Feth, M., 1979. Radiative cooling experiments on lunar glass analogues. In: 10th Proc. Lunar Planet. Sci. Conf, pp. 355–373. <https://adsabs.harvard.edu/pdf/1979LPSC...10...355A>.
- Bernard, O., Li, W.R., Costa, F., Saunders, S., Itikarai, I., Sindang, M., Maisonneuve, C.B., 2022. Explosive-effusive-explosive: the role of magma ascent rates and paths in modulating caldera eruptions. *Geology* 50, 1013–1017. <https://doi.org/10.1130/G50023.1>.
- Brown, G.M., Peckett, A., Emeleus, C.H., Phillips, R., Pinent, R.H., 1975. Petrology and mineralogy of Apollo 17 mare basalts. In: Proc. Lunar Sci. Conf. 6th, pp. 1–13. <https://adsabs.harvard.edu/pdf/1975LPSC...6....1B>.
- Brugman, K., Till, C.B., Bose, M., 2022. Common assumptions and methods yield overestimated diffusive timescales, as exemplified in a Yellowstone post-caldera lava. *Contrib. Mineral. Petrol.* 177, 63. <https://doi.org/10.1007/s00410-022-01926-5>.
- Chakraborty, S., Dohmen, R., 2022. Diffusion chronometry of volcanic rocks: looking backward and forward. *Bull. Volcanol.* 84, 57. <https://doi.org/10.1007/s00445-022-01565-5>.
- Che, X., Nemchin, A., Liu, D., Long, T., Wang, C., Norman, M.D., Joy, K.H., Tartese, R., Head, J., Jolliff, B., Snape, J.F., Neal, C.R., Whitehouse, M.J., Crow, C., Benedix, G., Jourdan, F., Yang, Z., Yang, C., Liu, J., Xie, S., Bao, Z., Fan, R., Li, D., Li, Z., Webb, S. G., 2021. Age and composition of young basalts on the moon, measured from samples returned by Chang'e-5. *Science* 374, 887–890. <https://doi.org/10.1126/science.abl7957>.
- Chen, Y., Li, C., Ren, X., Liu, J., Wu, Y., Lu, Y., Cai, W., Zhang, X., 2018. The thickness and volume of young basalts within Mare Imbrium. *J. Geophys. Res. Planets* 123, 630–645. <https://doi.org/10.1002/2017JE005380>.
- Costa, F., Dohmen, R., Chakraborty, S., 2008. Time scales of magmatic processes from modeling the zoning patterns of crystals. *Rev. Mineral. Geochem.* 69, 545–594. <https://doi.org/10.2138/rmg.2008.69.14>.
- Costa, F., Shea, T., Ubide, T., 2020. Diffusion chronometry and the timescales of magmatic processes. *Nat. Rev. Earth. Environ.* 1, 201–214. <https://doi.org/10.1038/s43017-020-0038-x>.
- Dohmen, R., Faak, K., Blundy, J.D., 2017. Chronometry and speedometry of magmatic processes using chemical diffusion in olivine, plagioclase and pyroxenes. *Rev. Mineral. Geochem.* 83, 535–575. <https://doi.org/10.2138/rmg.2017.83.16>.
- Donaldson, C.H., Usselman, T.M., Williams, R.J., Lofgren, G.E., 1975. Experimental modeling of the cooling history of Apollo 12 olivine basalts. In: 6th Lunar Sci. Conf. Proc, pp. 843–869. <https://hdl.handle.net/20.500.11753/1554>.
- Donohue, P.H., Neal, C.R., 2015. Quantitative textural analysis of ilmenite in Apollo 17 high-titanium mare basalts. *Geochim. Cosmochim. Acta* 149, 115–130. <https://doi.org/10.1016/j.gca.2014.11.002>.
- Du, J., Fa, W., Wicczorek, M.A., Xie, M., Cai, Y., Zhu, M.-H., 2019. Thickness of lunar mare basalts: new results based on modeling the degradation of partially buried craters. *J. Geophys. Res. Planets* 124, 2430–2459. <https://doi.org/10.1029/2018JE005872>.
- Du, J., Fa, W., Gong, S., Liu, Y., Qiao, L., Tai, Y., Zhang, F., Zou, Y., 2022. Thicknesses of Mare basalts in the Chang'E-5 landing region: implications for the late-stage volcanism on the moon. *J. Geophys. Res. Planets* 127. <https://doi.org/10.1029/2022JE007314>.
- Faak, K., Chakraborty, S., Coogan, L.A., 2013. Mg in plagioclase: experimental calibration of a new geothermometer and diffusion coefficients. *Geochim. Cosmochim. Acta* 123, 195–217. <https://doi.org/10.1016/j.gca.2013.05.009>.
- Faak, K., Coogan, L.A., Chakraborty, S., 2014. A new Mg-in-plagioclase geospeedometer for the determination of cooling rates of mafic rocks. *Geochim. Cosmochim. Acta* 140, 691–707. <https://doi.org/10.1016/j.gca.2014.06.005>.
- Fagents, S.A., Gregg, T.K.P., Lopes, R.M.C., 2013. Modeling Volcanic Processes: The Physics and Mathematics of Volcanism. Cambridge University Press. <https://doi.org/10.1017/CBO9781139021562>.
- Gagnepain-Beyneix, J., Lognonné, P.H., Chenet, H., Lombardi, D., Spohn, T., 2006. A seismic model of the lunar mantle and constraints on temperature and mineralogy. *Phys. Earth Planet. Inter.* 159, 140–166. <https://doi.org/10.1016/j.pepi.2006.05.009>.
- Ganguly, J., Dasgupta, S., Cheng, W., Neogi, S., 2000. Exhumation history of a section of the Sikkim Himalayas, India: records in the metamorphic mineral equilibria and compositional zoning of garnet. *Earth Planet. Sci. Lett.* 183, 471–486. [https://doi.org/10.1016/S0012-821X\(00\)00280-6](https://doi.org/10.1016/S0012-821X(00)00280-6).
- Gao, Y., Snow, J.E., Casey, J.F., Yu, J.B., 2011. Cooling-induced fractionation of mantle Li isotopes from the ultraslow-spreading Gakkal Ridge. *Earth Planet. Sci. Lett.* 301, 231–240. <https://doi.org/10.1016/j.epsl.2010.11.003>.
- Grove, T.L., 1982. Use of exsolution lamellae in lunar clinopyroxenes as cooling rate speedometers: an experimental calibration. *Am. Mineral.* 67, 251–268. <https://pubs.geoscienceworld.org/msa/ammin/article/67/3-4/251/41355/>.
- Grove, T.L., Walker, D., 1977. Cooling histories of Apollo 15 quartz-normative basalts. In: 8th Lunar Sci. Conf. Proc, pp. 1501–1520. <https://adsabs.harvard.edu/full/record/seri/LPSC./0008/1977LPSC...8.1501G.html>.
- Gudmundsson, A., 2020. Dynamics of volcanic eruptions. In: Gudmundsson, A. (Ed.), *Volcanotectonics: Understanding the Structure, Deformation, and Dynamics of Volcanoes*. Cambridge University Press, pp. 379–423.
- Hahn, T.M., Lunning, N.G., McSween, H.Y., Bodnar, R.J., Taylor, L.A., 2017. Dacite formation on Vesta: partial melting of the eucritic crust. *Meteorit. Planet. Sci.* 52, 1173–1196. <https://doi.org/10.1111/maps.12870>.
- Hartley, M.E., Morgan, D.J., MacLennan, J., Edmonds, M., Thordarson, T., 2016. Tracking timescales of short-term precursors to large basaltic fissure eruptions through Fe–Mg

- diffusion in olivine. *Earth Planet. Sci. Lett.* 439, 58–70. <https://doi.org/10.1016/j.epsl.2016.01.018>.
- He, Q., Li, Y., Baziotis, I., Qian, Y., Xiao, L., Wang, Z., Zhang, W., Luo, B., Neal, C.R., Day, J.M.D., Pan, F., She, Z., Wu, X., Hu, Z., Zong, K., Wang, L., 2022. Detailed petrogenesis of the unsampled Oceanus Procellarum: the case of the Chang'e-5 mare basalts. *Icarus* 383, 115082. <https://doi.org/10.1016/j.icarus.2022.115082>.
- Hiesinger, H., Head, J.W., Wolf, U., Jaumann, R., Neukum, G., 2002. Lunar mare basalt flow units: thicknesses determined from crater size-frequency distributions. *Geophys. Res. Lett.* 29, 84–89. <https://doi.org/10.1029/2002GL014847>.
- Hiesinger, H., Head, J.W., Wolf, U., Jaumann, R., Neukum, G., 2011. Ages and stratigraphy of lunar mare basalts: a synthesis. *Spec. Pap. Geol. Soc. Am.* 477, 1–51.
- Hu, X.Y., Chen, Y., Zhang, Y.Y., Li, S.L., Xia, X.Q., Wu, Y.Z., 2019. The thickness and scale of late-stage basalts in oceanus procellarum. *Chin. J. Astron. Astrophys.* 43 (1), 75–92. <https://doi.org/10.1016/j.chinastron.2019.02.002>.
- Hudgins, J.A., Spray, J.G., Hawkes, C.D., 2011. Element diffusion rates in lunar granitic breccias: evidence for contact metamorphism on the Moon. *Am. Mineral.* 96, 1673–1685. <https://doi.org/10.2138/am.2011.3640>.
- Hui, H., Peslier, A.H., Lapen, T.J., Shafer, J.T., Brandon, A.D., Irving, A.J., 2011. Petrogenesis of basaltic shergottite Northwest Africa 5298: closed-system crystallization of an oxidized mafic melt: Petrogenesis of Northwest Africa 5298. *Meteorit. Planet. Sci.* 46, 1313–1328. <https://doi.org/10.1111/j.1945-5100.2011.01231.x>.
- Ishihara, Y., Morota, T., Nakamura, R., Goossens, S., Sasaki, S., 2011. Anomalous Moscoviense basin: single oblique impact or double impact origin? *Geophys. Res. Lett.* 38, L03201. <https://doi.org/10.1029/2010GL045887>.
- Jaeger, J.C., 1957. The temperature in the neighborhood of a cooling intrusive sheet. *Am. J. Sci.* 255, 306–318. <https://doi.org/10.2475/ajs.255.4.306>.
- Jia, B., Fa, W., Xie, M., Tai, Y., Liu, X., 2021. Regolith properties in the Chang'E-5 landing region of the Moon: results from multi-source. *Remote Sens. Observ. J. Geophys. Res. Planets* 126. <https://doi.org/10.1029/2021JE006934> e2021JE006934.
- Jia, B., Fa, W., Zhang, M., Di, K., Xie, M., Tai, Y., Li, Y., 2022. On the provenance of the Chang'E-5 lunar samples. *Earth Planet. Sci. Lett.* 596, 117791 <https://doi.org/10.1016/j.epsl.2022.117791>.
- Jiang, Y., Li, Y., Liao, S., Yin, Z., Hsu, W., 2021. Mineral chemistry and 3D tomography of a Chang'E 5 high-Ti basalt: implication for the lunar thermal evolution history. *Sci. Bull.* <https://doi.org/10.1016/j.scib.2021.12.006>.
- Jones, R., Libourel, G., Villeneuve, J., 2018. Thermal histories of chondrules: Petrologic observations and experimental constraints. In: *Chondrules and the Protoplanetary Disk*. Cambridge University Press. <https://doi.org/10.1017/9781108284073.003>.
- Joy, K.H., Crawford, I.A., Anand, M., Greenwood, R.C., Franchi, I.A., Russell, S.S., 2008. The petrology and geochemistry of Miller Range 05035: A new lunar gabbroic meteorite. *Geochim. Cosmochim. Acta* 72, 3822–3844. <https://doi.org/10.1016/j.gca.2008.04.032>.
- Khan, A., Connolly, J.A.D., Pommier, A., Noir, J., 2014. Geophysical evidence for melt in the deep lunar interior and implications for lunar evolution. *J. Geophys. Res. Planets* 119, 2197–2221. <https://doi.org/10.1002/2014JE004661>.
- Li, Q.L., Zhou, Q., Liu, Y., Xiao, Z.Y., Lin, Y.T., Li, J.H., Ma, H.X., Tang, G.Q., Guo, S., Tang, X., Yuan, J.Y., Li, J., Wu, F.Y., Ouyang, Z.Y., Li, C.L., Li, X.H., 2021. Two-billion-year-old volcanism on the Moon from Chang'e-5 basalts. *Nature* 600, 54–58. <https://doi.org/10.1038/s41586-021-04100-2>.
- Li, C., Hu, H., Yang, M.-F., Pei, Z.-Y., Zhou, Q., Ren, X., Liu, B., Liu, D., Zeng, X., Zhang, G., Zhang, H., Liu, J., Wang, Q., Deng, X., Xiao, C., Yao, Y., Xue, D., Zuo, W., Su, Y., Wen, W., Ouyang, Z., 2022. Characteristics of the lunar samples returned by the Chang'E-5 mission. *Natl. Sci. Rev.* 9, nwab188. <https://doi.org/10.1093/nsr/nwab188>.
- Lierenfeld, M.B., Zhong, X., Reusser, E., Kunze, K., Putlitz, B., Ulmer, P., 2019. Species diffusion in clinopyroxene solid solution in the diopside-anorthite system. *Contrib. Mineral. Petrol.* 174, 46. <https://doi.org/10.1007/s00410-019-1571-9>.
- Liu, Y., Floss, C., Day, J.M.D., Hill, E., Taylor, L.A., 2009. Petrogenesis of lunar mare basalt meteorite MIL 05035. *Meteorit. Planet. Sci.* 44, 261–284. <https://doi.org/10.1111/j.1945-5100.2009.tb00733.x>.
- Lofgren, G.E., Usselman, T.M., Donaldson, C., 1975. Cooling history of Apollo 15 quartz normative basalts determined from cooling rate experiments. In: *6th Lunar Sci. Conf. Proc.* p. 515. <https://adsabs.harvard.edu/pdf/1975LPI....6.515L>.
- Lofgren, G.E., Irving, A.J., Bence, A.E., Lipman, P.W., Duke, M.B., Naldrett, A.J., Dungan, M.A., Papike, J.J., Green, J.C., Reid, A.M., Haggerty, S.E., Rhodes, J.M., Haskin, L.A., Taylor, S.R., Vaniman, D.T., 1981. Petrology and chemistry of terrestrial, lunar and meteoritic basalts. In: *Basaltic Volcanism on the Terrestrial Planets*, pp. 1–437.
- Long, T., Qian, Y., Norman, M.D., Miljkovic, K., Crow, C., Head, J.W., Che, X., Tartèse, R., Zellner, N., Yu, X., Xie, S., Whitehouse, M., Joy, K.H., Neal, C.R., Snape, J.F., Zhou, G., Liu, S., Yang, C., Yang, Z., Wang, C., Xiao, L., Liu, D., Nemchin, A., 2022. Constraining the formation and transport of lunar impact glasses using the ages and chemical compositions of Chang'e-5 glass beads. *Sci. Adv.* 8, eabq2542. <https://doi.org/10.1126/sciadv.abq2542>.
- McCallum, I.S., O'Brien, H.E., 1996. Stratigraphy of the lunar highland crust: depths of burial of lunar samples from cooling-rate studies. *Am. Mineral.* 81, 1166–1175. <https://doi.org/10.2138/am-1996-9-1015>.
- McCallum, S., Domeneghetti, M.C., Schwartz, J.M., Mullen, E.K., Zema, M., Cámara, F., McCammon, C., Ganguly, J., 2006. Cooling history of lunar Mg-suite gabbroic 76255, troctolite 76535 and Stillwater pyroxenite SC-936: the record in exsolution and ordering in pyroxenes. *Geochim. Cosmochim. Acta* 70, 6068–6078. <https://doi.org/10.1016/j.gca.2006.08.009>.
- Mikouchi, T., Makishima, J., Kurihara, T., Hoffmann, V.H., Miyamoto, M., 2012. Relative burial depth of nakhlites revisited. In: *Proceedings of the 43rd Lunar and Planetary Science Conference*. abstr. #2363. <https://ui.adsabs.harvard.edu/abs/2012LPL....43.2363M/abstract>.
- Mikouchi, T., Miyamoto, M., Comparative cooling rates of nakhlites as inferred from iron-magnesium and calcium zoning of olivines. [http://www.meteorite.fr/en/pdf/NWA817\\_1343.pdf](http://www.meteorite.fr/en/pdf/NWA817_1343.pdf).
- Mitsui, T., Rose, M.K., Fomin, E., Ogletree, D.F., Salmeron, M., 2002. Water diffusion and clustering on Pd(111). *Science* 297, 1850–1852. <https://doi.org/10.1126/science.1075095>.
- Miyamoto, M., Takeda, H., 1994. Evidence for excavation of deep crustal material of a Vesta-like body from Ca compositional gradients in pyroxene. *Earth Planet. Sci. Lett.* 122, 343–349. [https://doi.org/10.1016/0012-821X\(94\)90007-8](https://doi.org/10.1016/0012-821X(94)90007-8).
- Morgan, D.J., Blake, S., 2006. Magmatic residence times of zoned phenocrysts: introduction and application of the binary element diffusion modelling (BEDM) technique. *Contrib. Mineral. Petrol.* 151, 58–70. <https://doi.org/10.1007/s00410-005-0045-4>.
- Müller, T., Dohmen, R., Ter Heege, J., Chakraborty, S., 2013. Fe–Mg interdiffusion rates in clinopyroxene: experimental data and implications for Fe–Mg exchange geothermometers. *Contrib. Mineral. Petrol.* 166, 1563–1576. <https://doi.org/10.1007/s00410-013-0941-y>.
- Murri, M., Domeneghetti, M.C., Fioretti, A.M., Nestola, F., Vetere, F., Perugini, D., Pisello, A., Faccenda, M., Alvaro, M., 2019. Cooling history and emplacement of a pyroxenitic lava as proxy for understanding Martian lava flows. *Sci. Rep.* 9, 1–7. <https://doi.org/10.1038/s41598-019-53142-0>.
- Neal, C.R., Valenciano, J.L., Che, X., Shi, Y., Liu, D., Tao, L., Joy, K.H., Snape, J.F., Tartèse, R., Head, J., Jolliff, B., Nemchin, A., Norman, D., 2022. Crystal size distribution of ilmenite in Chang'E-5 basalt clasts. In: *Proceedings of the 53rd Lunar and Planetary Science Conference*, abstr. #2353. <https://ui.adsabs.harvard.edu/abs/2022LPLCo2678.2353N/abstract>.
- Oeser, M., Dohmen, R., Horn, I., Schuth, S., Weyer, S., 2015. Processes and time scales of magmatic evolution as revealed by Fe–Mg chemical and isotopic zoning in natural olivines. *Geochim. Cosmochim. Acta* 154, 130–150. <https://doi.org/10.1016/j.gca.2015.01.025>.
- Papike, J.J., Hodges, F.N., Bence, A.E., Cameron, M., Rhodes, J.M., 1976. Mare basalts: crystal chemistry, mineralogy, and petrology. *Rev. Geophys.* 14, 475–540. <https://doi.org/10.1029/RG014i004p00475>.
- Peck, D.L., Hamilton, S.H., Shaw, H.R., 1977. Numerical analysis of lava lake cooling models: part II, application to Alae lava lake, Hawaii. *Am. J. Sci.* 277, 415–437. <https://doi.org/10.2475/ajs.277.4.415>.
- Pelullo, C., Chakraborty, S., Cambeses, A., Dohmen, R., Arienzo, I., D'Antonio, M., Pappalardo, L., Petrosino, P., 2022. Insights into the temporal evolution of magma plumbing systems from compositional zoning in clinopyroxene crystals from the Agnane-Monte Spina Plinian eruption (Campi Flegrei, Italy). *Geochim. Cosmochim. Acta* 328, 185–206. <https://doi.org/10.1016/j.gca.2022.04.007>.
- Putirka, K.D., 2008. Thermometers and barometers for volcanic systems. *Rev. Mineral. Geochem.* 69, 61–120. <https://doi.org/10.2138/rmg.2008.69.3>.
- Qian, Y.Q., Xiao, L., Zhao, S.Y., Zhao, J.N., Huang, J., Flahaut, J., Martinot, M., Head, J.W., Hiesinger, H., Wang, G.X., 2018. Geology and scientific significance of the Rümker Region in northern Oceanus Procellarum: China's Chang'E-5 landing region. *J. Geophys. Res. Planets* 123. <https://doi.org/10.1029/2018JE005595>.
- Qian, Y.Q., Xiao, L., Head, J.W., Wilson, L., 2021a. The long sinuous Rille System in Northern Oceanus Procellarum and its relation to the Chang'e-5 returned samples. *Geophys. Res. Lett.* 48. <https://doi.org/10.1029/2021GL092663> e2021GL092663.
- Qian, Y.Q., Xiao, L., Head, J.W., van der Bogert, C.H., Hiesinger, H., Wilson, L., 2021b. Young lunar mare basalts in the Chang'e-5 sample return region, northern Oceanus Procellarum. *Earth Planet. Sci. Lett.* 555, 116702 <https://doi.org/10.1016/j.epsl.2020.116702>.
- Richter, F., Chaussidon, M., Mendybaev, R., Kite, E., 2016. Reassessing the cooling rate and geologic setting of Martian meteorites MIL 03346 and NWA 817. *Geochim. Cosmochim. Acta* 182, 1–23. <https://doi.org/10.1016/j.gca.2016.02.020>.
- Richter, F., Saper, R.M., Villeneuve, J., Chaussidon, M., Watson, E.B., Davis, A.M., Mendybaev, R.A., Simon, S.B., 2021. Reassessing the thermal history of martian meteorite Shergotty and Apollo mare basalt 15555 using kinetic isotope fractionation of zoned minerals. *Geochim. Cosmochim. Acta* 295, 265–285. <https://doi.org/10.1016/j.gca.2020.11.002>.
- Sakatani, N., Ogawa, K., Arakawa, M., Tanaka, S., 2018. Thermal conductivity of lunar regolith simulant JSC-1A under vacuum. *Icarus* 309, 3–24. <https://doi.org/10.1016/j.icarus.2018.02.027>.
- Sanford, R.F., Huebner, J.S., 1979. Reexamination of diffusion processes in 77115 and 77215. In: *10th Proc. Lunar Planet. Sci. Conf.* pp. 1052–1054. <https://adsabs.harvard.edu/pdf/1979LPI....10.1052S>.
- Self, S., Keszthelyi, L., Thordarson, T., 1998. The importance of pahoehoe. *Annu. Rev. Earth Planet. Sci.* 26, 81–110. <https://doi.org/10.1146/annurev.earth.26.1.81>.
- Shea, T., Lynn, K.J., Garcia, M.O., 2015. Cracking the olivine zoning code: distinguishing between crystal growth and diffusion. *Geology* 43, 935–938. <https://doi.org/10.1130/G37082.1>.
- Shearer, C.K., Hess, P.C., Wiczorek, M.A., Pritchard, M.E., Parmentier, E.M., Borg, L.E., Longhi, J., Elkins-Tanton, L.T., Neal, C.R., Antonenko, I., Canup, R.M., Halliday, A.N., Grove, T.L., Hager, B.H., Lee, D.C., Wiechert, U., 2006. Thermal and magmatic evolution of the Moon. *Rev. Mineral. Geochem.* 60, 365–518. <https://doi.org/10.2138/rmg.2006.60.4>.
- Stadermann, A.C., Jolliff, B.L., Krawczynski, M.J., Hamilton, C.W., Barnes, J.J., 2022. Analysis and experimental investigation of Apollo sample 12032, 366-18, a chemically evolved basalt from the Moon. *Meteorit. Planet. Sci.* 57, 794–816. <https://doi.org/10.1111/maps.13795>.

- Stanin, F.T., Taylor, L.A., 1979. Armalcolite/ilmenite-mineral chemistry, paragenesis, and origin of textures. In: 10th Lunar Sci. Conf. Proc, pp. 383–405. <https://adsabs.harvard.edu/pdf/1979LPSC...10..383S>.
- Streck, M.J., 2008. Mineral textures and zoning as evidence for open system processes. *Rev. Mineral. Geochem.* 69, 595–622. <https://doi.org/10.2138/rmg.2008.69.15>.
- Taylor, L.A., Onorato, P.I.K., Uhlmann, D.R., 1977. Cooling rate estimations based on kinetic modelling of Fe-Mg diffusion in olivine. In: 8th Proc. Lunar Planet. Sci. Conf, pp. 1581–1592. <https://adsabs.harvard.edu/pdf/1977LPSC....8.1581T>.
- Tian, H.C., Wang, H., Chen, Y., Yang, W., Zhou, Q., Zhang, C., Lin, H.L., Huang, C., Wu, S.T., Jia, L.H., Xu, L., Zhang, D., Li, X.G., Chang, R., Yang, Y.H., Xie, L.W., Zhang, D.P., Zhang, G.L., Yang, S.H., Wu, F.Y., 2021. Non-KREEP origin for Chang'e-5 basalts in the Procellarum KREEP Terrane. *Nature* 600, 59–63. <https://doi.org/10.1038/s41586-021-04119-5>.
- Toramaru, A., 2022. Cooling crystallization of magma. In: *Vesiculation and Crystallization of Magma. Advances in Volcanology*. Springer, Singapore. [https://doi.org/10.1007/978-981-16-4209-8\\_7](https://doi.org/10.1007/978-981-16-4209-8_7).
- Udry, A., Howarth, G.H., Lapen, T.J., Righter, M., 2017. Petrogenesis of the NWA 7320 enriched martian gabbroic shergottite: insight into the martian crust. *Geochim. Cosmochim. Acta* 204, 1–18. <https://doi.org/10.1016/j.gca.2017.01.032>.
- Vance, J.A., 1965. Zoning in igneous plagioclase: patchy zoning. *J. Geol.* 73, 636–651. <https://doi.org/10.1086/627099>.
- Walker, D., Longhi, J., Kirkpatrick, J., Hays, J.F., 1976. Differentiation of an Apollo 12 picrite magma. In: 7th Lunar Sci. Conf. Proc, pp. 1365–1389. <https://adsabs.harvard.edu/pdf/1976LPSC....7.1365W>.
- Wang, X., Hou, T., Wang, M., Zhang, C., Zhang, Z., Pan, R., Marxer, F., Zhang, H., 2021. A new clinopyroxene thermobarometer for mafic to intermediate magmatic systems. *Eur. J. Mineral.* 33, 621–637. <https://doi.org/10.5194/ejm-33-621-2021>.
- Webb, S., Neal, C.R., Che, X., Shi, Y., Liu, D., Tao, L., Joy, K.H., Snape, J.F., Tartèse, R., Head, J., Jolliff, B., Nemchin, A., Norman, D., 2022. Crystal size distribution of plagioclase in basalt fragments from oceanus procellarum recovered by Chang'e-5. In: Proceedings of the 53rd Lunar and Planetary Science Conference, abstr. #2896. <https://ui.adsabs.harvard.edu/abs/2022LPICo2678.2896W/abstract>.
- Weider, S.Z., Crawford, I.A., Joy, K.H., 2010. Individual lava flow thicknesses in Oceanus Procellarum and Mare Serenitatis determined from Clementine multispectral data. *Icarus* 209, 323–336. <https://doi.org/10.1016/j.icarus.2010.05.010>.
- Wenzel, A., Filiberto, J., Stephen, N., Schwenzler, S.P., Hammond, S.J., 2021. Constraints on the petrologic history of gabbroic shergottite Northwest Africa 6963 from pyroxene zoning profiles and electron backscattered diffraction. *Meteorit. Planet. Sci.* 56, 1744–1757. <https://doi.org/10.1111/maps.13737>.
- Wesselink, A.J., 1948. Heat conductivity and nature of the lunar surface material. *Bull. Astron. Inst. Neth.* 10, 351–363. <https://adsabs.harvard.edu/pdf/1948BAN....10..351W>.
- Wieczorek, M.A., Phillips, R.J., 2000. The “Procellarum KREEP Terrane”: implications for mare volcanism and lunar evolution. *J. Geophys. Res. Planets* 105, 20417–20430. <https://doi.org/10.1029/1999JE001092>.
- Wieczorek, M.A., Jolliff, B.L., Khan, A., Pritchard, M.E., Weiss, B.P., Williams, L.L., Hood, L.L., Righter, K., Neal, C.R., Shearer Jr., C.K., McCallum, I.S., Tompkins, S., Hawke, B.R., Peterson, C.A., Gillis-Davis, J.J., Bussey, D.B.J., 2006. The constitution and structure of the lunar interior. In: *New Views of the Moon*. Mineralogical Society of America. <https://doi.org/10.2138/rmg.2006.60.3>.
- Wilson, L., Head, J.W., 2017. Generation, ascent and eruption of magma on the Moon: new insights into source depths, magma supply, intrusions and effusive/explosive eruptions (Part 2: predicted emplacement processes and observations). *Icarus* 283, 176–223. <https://doi.org/10.1016/j.icarus.2016.05.031>.
- Wilson, L., Head, J.W., Qian, Y., Xiao, L., 2022. Modeling the eruption of the lavas sampled by the Chang'e 5 mission. In: Proceedings of the 53rd Lunar and Planetary Science Conference, abstr. #1624. <https://ui.adsabs.harvard.edu/abs/2022LPICo2678.1624W/abstract>.
- Winkler, H.G.F., 1949. Crystallization of basaltic magma as recorded by variation of crystal-size in dikes. *Mineral. Mag. J. Mineral. Soc.* 28, 557–574. <https://doi.org/10.1180/minmag.1949.028.205.04>.
- Xue, Z., Welsh, D.F., Neal, C.R., Xiao, L., 2021. Understanding the textures of Apollo 11 high-Ti mare basalts: A quantitative petrographic approach. *Meteorit. Planet. Sci.* 56, 2211–2229. <https://doi.org/10.1111/maps.13767>.
- Yamaguchi, A., Barrat, J.A., Chaussidon, M., Beck, P., Villeneuve, J., Byrne, D.J., Broadley, M.W., Marty, B., 2021. Petrology and geochemistry of Erg Chech 002, the oldest andesite in the solar system. In: Proceedings of the 52nd Lunar and Planetary Science Conference, abstr. #1892. <https://ui.adsabs.harvard.edu/abs/2021LPI....52.1892Y/abstract>.
- Yang, X., Fa, W., Du, J., Xie, M., Liu, T., 2021. Effect of topographic degradation on small lunar craters: implications for regolith thickness estimation. *Geophys. Res. Lett.* 48. <https://doi.org/10.1029/2021GL095537> e2021GL095537.
- Yue, Z.Y., Di, K.C., Wan, W.H., Liu, Z.Q., Gou, S., Liu, B., Peng, M., Wang, Y.X., Jia, M.N., Liu, J.Z., Ouyang, Z.Y., 2022. Updated lunar cratering chronology model with the radiometric age of Chang'e-5 samples. *Nat. Astron.* 6, 541–545. <https://doi.org/10.1038/s41550-022-01604-3>.
- Zhang, Y., 2010. Diffusion in minerals and melts: theoretical background. *Rev. Mineral. Geochem.* 72, 5–59. <https://doi.org/10.2138/rmg.2010.72.2>.
- Zhang, N., Parmentier, E.M., Liang, Y., 2013. Effects of lunar cumulate mantle overturn and megaregolith on the expansion and contraction history of the Moon. *Geophys. Res. Lett.* 40, 5019–5023. <https://doi.org/10.1002/grl.50988>.
- Zhang, B., Ge, J., Xiong, Z., Zhai, S., 2019. Effect of water on the thermal properties of olivine with implications for lunar internal temperature. *J. Geophys. Res.: Planets* 124, 3469–3481. <https://doi.org/10.1029/2019JE006194>.
- Zhang, W.B., Zhang, N., Li, H.Y., 2022. Abundances of lunar heat-producing elements constrained by a 3-D numerical model of titanium-rich basaltic eruption. *Chin. J. Geophys.* 65 (1), 119–136. <https://doi.org/10.6038/cjg2022P0753>.